# CONTROL OF CONTACT CHARGING ON POLYMERS
# WITH
# ORGANIC CHARGE-TRANSFER COMPLEXES
# AND
# QUANTUM DOTS

A THESIS SUBMITTED TO
THE GRADUATE SCHOOL OF ENGINEERING AND SCIENCE
OF BILKENT UNIVERSITY
IN PARTIAL FULFILLMENT OF THE REQUIREMENTS FOR
THE DEGREE OF
MASTER OF SCIENCE IN
MATERIALS SCIENCE AND NANOTECHNOLOGY

By
Sunay Dilara EKİM
August 2022

# Control of Contact Charges on Polymers with Organic Charge-Transfer Complexes and Quantum Dots

By Sunay Dilara Ekim

August 2022

We certify that we have read the thesis and that, in our opinion, it is fully adequate, in scope and in quality, as a thesis for the degree of Master of Science.

Bilge BAYTEKİN (Advisor)

Demet Asil ALPTEKİN

Ferdi KARADAŞ

Approved for the Graduate School of Engineering and Science:

Director of the Graduate School
Orhan ARIKAN

# ABSTRACT

## Control of Contact Charging on Polymers with Organic Charge-Transfer Complexes and Quantum Dots

Sunay Dilara Ekim
M.S. in Materials Science and Nanotechnology
Advisor: Bilge BAYTEKIN
August 2022

Contact charging, also known as triboelectrification, occurs when two insulator materials are contacted and separated. The mechanism of polymer triboelectrification and the following charge dissipation are still 'mysteries' in the current scientific research. However, generation and transfer of contact charges on surfaces could be harmful to many industries. It causes substantial economic losses in, e.g., space industry where satellites are damaged, in pharmaceuticals where charging of powder drugs is a severe problem for process and manufacturing, and in microelectronics where MEMs devices suffer from triboelectric charging. So far, the common approach to this problem is to render surfaces conductive with high loading of conductive additives, which is not ideal for most of the industrial applications. This thesis presents some efforts to open and explore new light-controlled discharging mechanisms for contact-charges on polymers, without an increase in surface conductivity of the polymer surface. The antistatic behavior of the polymer surfaces are achieved by doping of organic charge-transfer complexes (CTC)s or quantum dots (CdSe, CdSe/ZnSe). In the first part of the study, the CTCs formed from pyrene and its derivatives, and TCNQ doped into the polydimethylsiloxane (PDMS) were found to affect a faster discharge compared to the discharging on undoped polymers, as monitored by Faraday cup measurements. In a second setup, solutions of CTCs dropped into the vials of contact charged polymer beads in hexane affected a similar faster discharge of the beads, which was monitored by the fall time of the beads. In both solid samples and with the beads in hexane, the time required for the polymer discharge mediated by each CTC was related to the CTCs degree of charge transfer. Additionally, when the samples were excited by a UV source, the charge decays were faster in comparison to the non-illuminated samples. Theoretical calculations confirmed that HOMO-LUMO gap decreases upon excitation, which enhances the dissipation of tribocharges. It was also found that hydrogen bonds between donor and acceptor moieties alter the CTC morphology in PDMS, which yields differences in charging and discharging behavior. The formed CTC-composites were characterized by UV-Vis, AFM, XRD, and SEM. In the second part of this thesis, CdSe, CdSe/ZnSe quantum dots (QD) were doped in the polymers to test the polymer discharging performance of these materials. The formed QD-composites were characterized by UV-Vis, TRF, XRD, SEM, and TEM. This new set of materials bring in their unique properties to the polymer composites, i.e., bandgaps which are tunable, and quantum confinement effects in the nanocrystals. These properties unlatch new doors to the charge dissipation, one of which was explored by changing spatial delocalization of holes and electrons in semiconductors with band-gap engineering.

In this study, the faster discharging on polymers doped with CTCs and QDs affected by a control of their properties, like degree of charge transfer (for CTC) and hole-electron localizations (QD) were displayed. It was shown that light-controlled remote discharging maybe expanded to other types of materials, and it can be fine-tuned by materials' properties.  The results point towards other possible but yet unexplored discharging mechanisms with unconventional additives, which do not simply increase the polymers' surface conductivity. Finally, we believe that these findings can be useful where materials are needed to be antistatic, but not conductive, such as in the electronic coatings.

# ÖZET

## Organik Yük-Transfer Kompleksleri ve Kuantum Noktaları ile Statik Elektriğin Kontrol Edilmesi

Sunay Dilara Ekim
Malzeme Bilimi ve Nanoteknoloji, Yüksek Lisans
Tez Danışmanı: Bilge BAYTEKIN
Ağustos 2022

Triboelektrik olarak da bilinen dokunma ile elektriklenme, iki yalıtkan malzeme birbirine temas ettiğinde ve ayrıldığında meydana gelir. Polimerlerde triboelektrik mekanizması ve yük sönümlenmesi mevcut bilimsel araştırmalarda hala bir gizemdir. Bununla birlikte, yüzeylerde statik elektrik birikimi ve sönümlenmesi birçok endüstri için zararlı olabilir. Örneğin, uyduların zarar gördüğü uzay endüstrisinde, toz ilaçların proses ve üretim süeçlerinde biriken statik elektrik ciddi bir sorundur ve MEMS cihazlarının triboelektriklenmeden muzdarip olduğu mikro elektronikte önemli ekonomik kayıplara neden olur. Şimdiye kadar, bu soruna ortak yaklaşım, endüstriyel uygulamaların çoğu için ideal olmayan yüksek iletken katkı maddeleri katkılanarak yüzeyleri iletken hale getirmektir. Bu tez, polimer yüzeyinin yüzey iletkenliğinde bir artış olmaksızın, polimerler üzerindeki temas yükleri için yeni ışık kontrollü sönümleme mekanizmalarını keşfetmek için araştırmalar sunmaktadır. Polimer yüzeylerin antistatik davranışı, organik yük transfer komplekslerinin (CTC) veya kuvantum noktalarının (CdSe, CdSe/ZnSe) katkılanmasıyla elde edilir. Çalışmanın ilk bölümünde, piren ve türevlerinden oluşturulan CTC'ler ve polidimetilsiloksan (PDMS) içine katkılı TCNQ'nun, Faraday kap ölçümleri ile izlendiği gibi, katkısız polimerlerdeki yük sönümlemesine kıyasla daha hızlı bir sönümleme gerçekleştirdiği bulundu. İkinci bir düzenekte, hekzan içindeki triboelektrik yüklü polimer boncukların şişelerine damlatılan CTC çözeltileri, boncukların düşme süresi ile boncukların daha hızlı yük sönümlemesini etkiledi. Hem katı numunelerde hem de hekzan içindeki boncuklarla, her bir CTC'nin aracılık ettiği polimer yük sönümlemesi için gereken süre, CTC'lerin yük transfer derecesi ile ilgilidir. Ek olarak, numuneler bir UV kaynağı tarafından uyarıldığında, ışıksız numunelere kıyasla yük azalmaları daha hızlı olmuştur. Teorik hesaplamalar, uyarım üzerine HOMO-LUMO aralığının azaldığını ve bu da tribo şarjların dağılmasını arttırdığını doğruladı. Verici ve alıcı kısımlar arasındaki hidrojen bağlarının PDMS'deki CTC morfolojisini değiştirdiği, bu da yükleme ve yük sönümleme davranışında farklılıklara neden olduğu bulundu. Oluşturulan CTCler UV-Vis, XRD, KPFM, ve SEM ile karakterize edildi. Bu tezin ikinci bölümünde, bu malzemelerin polimer yük sönümleme performansını test etmek için polimerlerde CdSe, CdSe/ZnSe kuantum noktaları (QD) katkılanmıştır. Sentezlenen ve oluşturulan QD ve QD-kompozitleri UV-Vis, XRD, TRF, SEM ve TEM ile karakterize edildi. Bu yeni malzeme seti, polimer kompozitlere benzersiz özelliklerini, yani ayarlanabilir bant boşluklarını ve nanokristallerdeki kuvantum hapsetme etkilerini getiriyor. Bu özellikler, yük dağılımına yeni kapılar açar; bunlardan biri, bant aralığı mühendisliği ile yarı iletkenlerdeki boşlukların ve elektronların uzamsal yer değiştirmesinin değiştirilmesiyle keşfedilmiştir.

Bu çalışmada, yük transfer derecesi (CTC için) ve electron-boşluk lokalizasyonları (QD) gibi özelliklerinin kontrolünden etkilenen CTC'ler ve QD'ler ile katkılı polimerler üzerinde daha hızlı triboelektrik yük sönümlendiği gösterildi. Işık kontrollü uzaktan yük sönümlemenin diğer malzeme türlerine genişletilebileceği ve malzemelerin özelliklerine göre ince ayar yapılabileceği gösterildi. Polimerlerin yüzey iletkenliğini artırmayan, geleneksel olmayan katkı maddeleri içeren diğer olası ancak henüz keşfedilmemiş yük sönümleme mekanizmalarını ortaya çıkardı. Son olarak, bu bulguların, elektronik kaplamalar gibi malzemelerin antistatik ancak iletken olmaması gereken durumlarda faydalı olabileceğine ve ilham kaynağı olabileceğine inanıyoruz.

## Acknowledgments

Many people have been invaluable in the completion of my master degree. First and foremost, I would like to thank my advisor, Assoc. Prof. Bilge Baytekin for accepting me in her group and guidance throughout my project. I am very grateful to Assist. Prof. H. Tarik Baytekin, while not formally an advisor, welcomed me to his laboratory to research and for countless of meetings. I would like to thank Assist. Dr. Erol Yildirim for his valuable theoretical calculations, his support and constructive feedback. I would like to also thank Assist. Prof. Demet Asil Alptekin for her valuable discussions and the preparation and supply of the QDs used in this study.

I would like to thank everyone in the Bilge Baytekin's group, especially Joanna Kwiczak Yiğitbasi, Görkem Eylul Kaya, and Elif Akbulut, for always being welcoming and helpful throughout my research in the lab. I thank to Murat Daştemir for the theoretical calculations he performed, and Firdevs Aydin for the QDs she synthesized.

I am grateful to all the jury members Assist. Prof. Demet Asil Alptekin and Assoc. Prof. Ferdi Karadaş for their time and feedback. I thank to the Scientific and Technological Research Council of Turkey (TUBITAK) for providing the research grant (120M694).

Finally and most importantly I thank to my extended and immediate family for their constant, never-ending love and support. This includes Yesim, Hikmet, Mert, Romeo and Bal Bocek Ekim, Gulizar Kocdemir, Elvan Sarcan, Oyku Yamanturk, Hulya Sarcan and Ilgin Kamanli. I thank my beloved friends, Busra Kabatas, Derya Bektas, Bartu Ayaz, Gizem Tezgel, and Goksu Sarioglu for their support and encouragement.

*For my mother, father, and Sisi,*

## Contents

## List of Figures

## List of Tables

*“Notwithstanding my experiments with electricity the thunderbolt continues to fall under our noses and beards; and as for the tyrant, there are a million of us still engaged at snatching away his sceptre”*

**Benjamin Franklin**

# Chapter 1

## 1. Introduction

### 1.1 What is Triboelectricity?

Electrostatic charges develop when two surfaces are contacted and separated. This phenomenon, contact electrification or triboelectrification, is not yet clearly understood. Triboelectricity was first discovered when human hair was electrified with amber, known as the ‘amber effect’ [1]. Static electricity is a natural phenomenon and manifests itself in different events in our daily lives. When a balloon is rubbed, it attracts and sticks to other materials. Our hair can get electrified upon friction between the hair and the comb, especially on dry days. Indeed, to mitigate charges on hair, positively charged surfactants and polymers are added to shampoos and conditioners [7]. Triboelectricity could occur between solid-solid, solid-liquid, liquid-liquid, liquid/gases, and solid/gases interfaces [2]. Accumulation of static charges may result in electrostatic discharging (ESD). Lightning is a form of ESD. Two materials -grounded or not grounded- may exchange their contact charges. You can feel a sudden shock of ESD when you touch a metal door knob after walking or rubbing your feet to the ground.

Contact charging can be used in (industrial) applications. In these applications, generated contact charges are used [3]. For example, mechanical energy harvesting nanogenerators known as TENGs use mechanical energy to develop triboelectric charging between contacting surfaces, which can be used in powering devices [4]. Electrophotography and electrostatic coating are other applications of contact charging [5] [6].

## 1.2 Triboelectric Series

Different materials, polymers, metals, semiconductors, and ceramics, can get charged by rubbing, friction, and contact. The triboelectric series, named by Shawn in 1917, is a guide for material selection based on the tendency of charges of materials [9]. JC Wilcke obtained the first triboelectric list in 1757 [8]. Then, many scientists, e.g., Faraday, Jamin, and Bouty, proposed their lists.

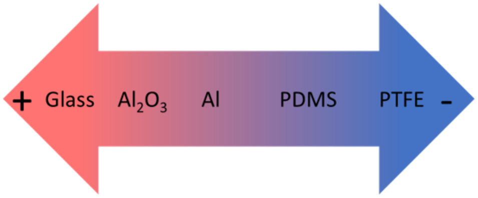

**Figure 1. 1.** An example of a triboelectric series of materials, adapted from [10] and [11].

Although the materials generally comply with the order in the triboelectric series, there are different series in the literature with materials in other orders. Different conditions in the experimental process, polymer processing history, contaminations in the samples, mechanical deformations on the sample surface, asymmetry in the mechanical contact, and material transfer during the contact are possible sources of these inconsistencies. In the last decade, it was shown that the charges on surfaces are neither all positive nor all negative. On the polymer surfaces, all materials have domains of positive and negative charges. The usual method of measuring contact charges at the macro scale displays a mathematical sum of the charges in these domains, which can turn out to be (minute) positive or negative depending on the regions selected for charge measurements [10], [37], and [39].

## 1.3 Proposed Mechanisms of Triboelectric Charge Generation and Dissipation

The mechanism of triboelectricity, which occurs at different interfaces and in different materials, is a matter of debate for scientists. Generally, an electron transfer mechanism is proposed for all contacts, leading to a false generalization and over-simplification of the complex phenomenon. This proposal is made because triboelectric studies are focused on the metal-metal or polymer-metal interfaces. However, if electron transfer is the cause of contact charging also in polymer-polymer contacts, where is the source of these transferred electrons in insulators - the materials for which the electrons are localized in the orbitals? This fundamental question led to discussing five charging mechanisms in connection with charging phenomena in recent years: electron transfer, ion transfer, material transfer, bond-breaking, and the combined mechanism. These mechanisms are illustrated in Figure 1.2.

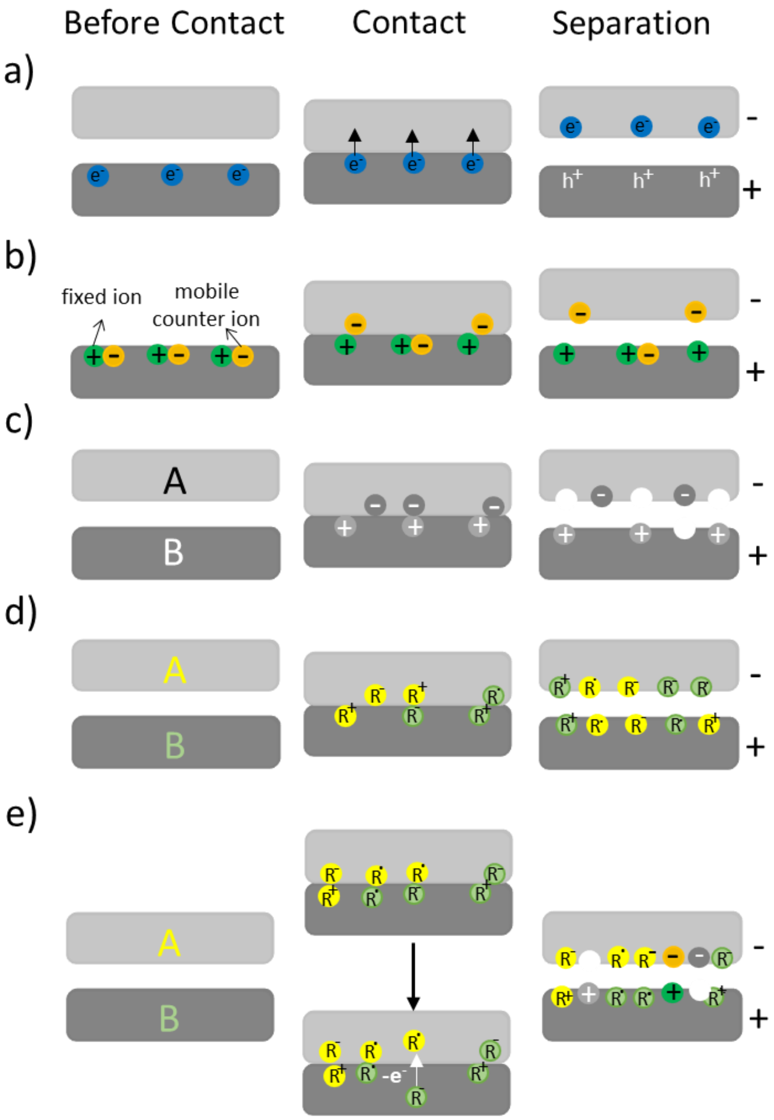

**Figure 1.2.** The schematic illustration of triboelectric mechanisms a) electron-transfer b) ion-transfer, c) material transfer, d) bond breaking mechanism, e) combined mechanism.

### 1.3.1 Electron transfer

Work function (Ø) is the energy required to remove an electron from a surface. When two metal surfaces are contacted, the electron flows from the material with a lower work function to the material with a higher work function. Fermi levels of the two surfaces are equalized, and thermodynamic equilibrium is created. **Figure 1.3** shows the electron transfer mechanism for metal-metal interfaces. A metal with a low work function (A) is charged positively because it gives electrons, and a metal with a high work function (B) is charged negatively because it receives electrons. Contact potential difference ($V_C$) is generated due to the flow of electrons between metal surfaces.

$$V_C = \frac{\Delta\emptyset}{e} = \frac{\emptyset_B - \emptyset_A}{e}$$

e is the charge on the electron (e=1.6 x $10^{-16}$ C) [12].

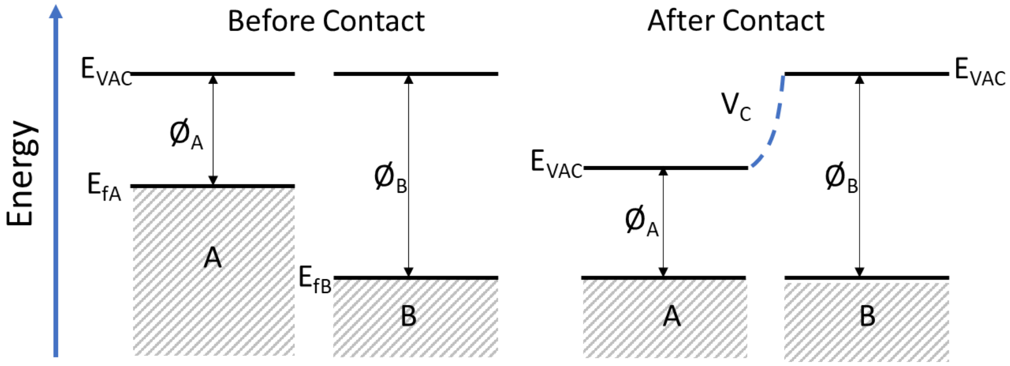

**Figure 1.3.** A schematic scheme of energy band diagram of two metals before contact and after contact

The gap between the highest occupied molecular orbital (HOMO) and the lowest unoccupied molecular orbital (LUMO) is very high for insulators. Due to this large gap, electron transfer does not occur in insulator surfaces in thermodynamic equilibrium. Lowell proposed that electron transfer in insulators occurs through localized states (traps) which shifts the energy, but these defects are insufficient to account for observed charging [13], [14], [15].

It has been shown that when perovskite crystalline structure surfaces are contact-charged, surface lattice deformations occur, creating surface dipoles. These surface dipoles create an electric field and enable electron transfer [16]. In a different study, it has been shown that electrons can be excited to the conduction band in semiconductors with small band gaps due to the friction during contact of the surfaces [17], [18]. Yet, there is no convincing study to provide evidence that polymers can undergo a direct electron transfer in triboelectrification [19].

### 1.3.2 Ion transfer

When Knoblauch contact-charged solid organic acids and bases with filter paper, solid organic acids were negatively charged, and solid organic bases were positively charged. He proposed the proton transfer mechanism for his observation [20]. Similarly, researchers found that the mechanism of contact electrification in some polymers was related to the acidity and basicity properties of the polymers. Medley studied acidic and basic ion exchange resins, and the same results with Knoblauch’s experiments were obtained [21]. Diaz, too, proposed the proton transfer mechanism to explain the triboelectric mechanism for some polymers [22].

Harper indicates that electron transfer cannot be the primary mechanism for insulators in contact electrification [23]. Some insulators, such as glass, have mobile ions, and the triboelectric mechanism can be explained by ion transfer. However, mobile ions are not found on every polymer surface, such as polyethylene. For such polymer surfaces, it is suggested that ion transfer from the atmosphere to such surfaces may occur. However, ion transfer could not be accounted for as the sole mechanism of contact charging, as the order of the triboelectric series did not change when the related experiments were carried out under different environmental conditions.

In ion-containing polymers, there are immobile ions and mobile counterions. Medley found a relationship between the sign of the immobile ion and the surface charge gained after contact electrification [24]. Then, Diaz showed a relationship between the ion concentration in the polymer and the amount of charge on these polymers [25].

In polymers without mobile ions, ions adsorbed from the atmosphere play a role in forming surface charge [26], [27]. Galembeck and Gouveia used Kelvin Probe Force Microscopy (KFM) to show that on hydrophilic surfaces, electrical potential changes with humidity [28].

Whitesides and McCarty proposed a new triboelectric series according to the tendency of $OH^-$ ion accumulation on the surfaces of the materials. [29]. They used the zheta ζ potential that reflects the amount of surface-accumulated ions from the liquid interface and is a measure of the surface charge. This potential is negative, possibly due to the accumulation of the $OH^-$ charge onto the surface of polymers. Still, the order of all polymers in the series is not consistent with the charging trend observed in the triboelectric series.

In summary, the effects of ion transfer between the polymers and the depositions of ions from the atmosphere on the surfaces on the surface charging and discharging of polymers have been demonstrated clearly and undoubtedly by many studies. However, the fact that common insulator polymers can still be contact-charged under high vacuum and under oil (without air or water to supply the ions) shows that the triboelectric mechanism cannot be explained only by ion transfer [30], [31], [19].

### 1.3.3 Material Transfer

Harper mentioned that material transfer might play a role in the contact electrification mechanism. He proposed that the transferred material has a different electrical potential and causes charging [32]. Salanek et al. provided the first experimental evidence for the mass transfer mechanism in contact electrification by analyzing the surfaces of contacting polymer pairs with a non-destructive characterization method, XPS [33]. Lowell showed that contact-charge formation is not affected by previous contacts using polymer-polymer and polymer-metal surfaces. Therefore, he implied that mass transfer could not be the primary mechanism [34] for the contact charging of the polymers. However, it was later shown that the prolonged contact and the increase in the material transfer amount could lead to drastic effects in the contact-charging of polymers, such as the polarity reversal of the charge on the polymer pieces from + to -, or vice versa [35], showing that this mechanism may dominate the other possible mechanisms on the outcome of the charging.

### 1.3.4 Bond Breaking

Henniker was the first person to reveal that the bonds in polymers can be broken due to friction and that the formed radicals play a role in contact electrification. While creating his triboelectric series, he stated that the mechanism that creates the material order of the series is not related to the material bonds' dipole moments, dielectric properties, or ultra-violet-trigerred luminescence. He emphasized that the series order depends on the chemical nature of polymers, their molecular structure, and their chemical nature on the surface [36]. Sakaguchi showed that mechanoradicals are formed during triboelectrification due to the chain scission, and there is a relationship between discharge begin and the initiation of the radical decay [37]. In later years, Baytekin et al. displayed that contact charges on common polymers can be dissipated by doping them with radical scavenger molecules such as diphenyl picrylhydrazyl (DPPH) [38].

### 1.3.5 Combined Mechanism

The mechanism of contact charging insulators is still an active subject of research and discussion. So far, the studies indicate that there is no convincing single mechanism of charging and discharging in contact charging of insulators. For example, considering only the electron transfer mechanism and the electronic properties of the polymers disregards both mechanochemical events and the importance of other material properties (such as mechanical properties). However, recent studies convincingly proved that the mechanical processes cause covalent bond breaking in the polymer chains and the consequent formation of mechanoanions, mechanocations, and mechanoradicals on the polymer surfaces [38]. According to the combined mechanism, bond scission is the first step that creates charged species on the surface. These species can interact electronically. During contact and separation, they can accept or donate their electrons to other species on the same surface or those on the contacting surface. Likewise, all the other mechanisms involving electron, ion, and material transfer can be related to the bond rupture and associated with each other in the combined mechanism hypothesis.

As a first implication of the combined mechanism hypothesis, Sakaguchi showed that electrons could transfer among mechanoanions, mechanocations, and mechanoradicals [39] Baytekin et al. imaged the contact charges on polymer surfaces by Kelvin Probe Force

Microscopy as positive and negative nanodomains forming a mosaic structure [40]. Gallembeck displayed the same type of mosaic of positive and negative charges on polymer surfaces at the macroscale [41]. Very recently, Ellis proved the relation between cohesive energy densities of the surfaces and their triboelectrification behavior [42]. In these studies, it is stated that the polymer bonds are cleaved during contact and separation, resulting in charged species (anions and cations) detected as contact charges. Then electron transfer can take place between these species, ion transfer or material transfer can occur between the surfaces.

## 1.4 Charge Dissipation Methods

Faster charge dissipation of polymers can be achieved by several methods. The commercialized conventional methods involve doping the polymers with additives to increase the surface conductivity [43], [44]. This increase can be achieved by increasing electrical conductivity by adding conducting additives, e.g., metals and metal nanoparticles, or increasing the amount of water adsorbed on the polymer surfaces by adding salts [45]. The latter can also be realized by oxidizing the surfaces of the polymers [46]. In the last decade, it has also shown an unconventional charge dissipation mechanism involving organic radical scavengers (e.g., tocopherol, diphenylpicryl hydrazyl, dopamine, and tannic acid) doped into the polymers [47], [48], [49]. With these studies, it was shown that it is also possible to render polymers antistatic without altering their conductivity. Later, it was also found that this radical scavenging mechanism is the basis of the antistatic behavior of wood, an insulator material [50]. In a previous study, Cezan et al. used light to dissipate charges on common polymers doped with organic dyes to control charge dissipation remotely [51]. This report stated that the higher the dipole moment of the excited dyes, the faster the charge dissipation.

## 1.5 Common Electrostatic Problems

Losses and explosions initiated by the contact charging and the electrostatic discharging (ESD) of the surfaces are more common than one would expect in the industry. Contact-charging of granular material and dust can cause rapid fires and dust explosions, which have been reported since the 18th century[10]. The problem related to ESD increased in number and type in the 20th century [10]. For example, in the production of synthetic films, fibers adhere to machine parts due to static electricity causing the production line to stop [52]. It has been documented by The Occupational Safety and Health Administration (OSHA) that different kinds of powder materials, milk, soy, apple, tobacco blend, charcoal, dextrin, and plastics, can cause flammable dust explosions [53]. In the pharmaceutical industry, dust is affected by static electricity and can cause non-homogenous mixtures to be produced [54]. Also, static electricity can reduce the efficiency of energy generation. Solar cell efficiency could be reduced due to static electricity of dust particles that stick to solar panels and block the sunlight [55]. ESD results in the breakdown of semiconductor electronic devices, computer boards, and electronic circuits in the electronic industry [56]. When dielectric fluids, e.g., gasoline, and hydrocarbons, flow in a pipe, they accumulate charges due to friction with the pipe walls. With the highly flammable vapor of the fluid, these charges can lead to fires and explosions [57]. To prevent all these problems, the mechanism of contact charging needs to be clarified, and protective measures must be designed accordingly. Insufficient understanding of the contact charging mechanism and the ill-defined, one-way view of this mechanism hampers the endeavors toward solutions. Also, specific solutions must be applied to various media and materials. Therefore it is necessary to increase the number of ‘antistatic’ resolutions and explore new ways of charge dissipation, rather than the simple ‘increase of the conductivity’ approach that is currently the most used one.

## 1.6 Thesis overview

In this thesis, we provide two new ways of dissipation of contact charges on common polymers by additives: 1) with organic charge transfer complexes (CTCs) and 2) with inorganic nanocrystals (quantum dots).

Part A examines the basic concept of charge transfer complexes and the contact charging and discharging effect of polymers doped with CTCs. Part B explores the basic idea of doping inorganic nanocrystals and their triboelectric effect on polymers.

The first chapter covers the concept of triboelectricity, including different theories of charge generation and discharging and the everyday problems of contact electrification in industry.

In Chapter 2, different experimental techniques used to measure the generated contact charges and the charge dissipation are introduced.

Chapter 3 introduces the basic concepts about charge transfer complexes, including their formation, crystal structure, and the importance of the charge transfer degree in their electronic properties. The CTCs used in this study are described.

In Chapter 4, we present the use of CTCs in the control of contact charging in PDMS. First, the preparation of charge transfer complexes and their characterization are introduced. Then, the effect of CTC on charge generation and dissipation in solid polymers and polymers in contact with CTC solutions are presented. We report that the decrease in HOMO-LUMO energy levels between acceptor and donor increases the affected charge dissipation. UV light enhances the dissipation of contact charges by reducing HOMO-LUMO energy levels of charge transfer complexes.

Chapter 5 describes the colloidal semiconductor nanocrystals, their preparation methods, their applications, and their classification.

Chapter 6 presents the preparation and characterization of quantum dots used in this thesis. The addition of these to the polymers and the effect of adding quantum dots to the charge dissipation on polymers are presented. We discuss the possible interplay between contact-charge decay and the (de)localization holes and electrons in the shell or core.

# Chapter 2

## 2. Materials, Setup, Measurement Devices, and Computational Methods

This chapter explains the materials used in the experiments and three different setups used to monitor the formation and dissipation of the triboelectric charge on these polymers. The first setup is a tapping device that records the charge formation as an open circuit potential created upon tapping the two surfaces. The second and third setups are for monitoring the charge dissipation, one for solid polymers in air, and the other for polymers in contact with the solution of the antistatic agent (CTC or QD, in this thesis).

## 2.1 Materials and Sample Preparation

Pyrene derivatives, TCNQ, and all solvents were purchased from Sigma Aldrich.

**Solid polymers.** Polydimethylsiloxane (PDMS) is a typical elastomer polymer used in contact-charging studies because of its ease in preparation (using elastomer kits). The flat PDMS surface, attained by curing the elastomer mixture (prepolymer) on a flat surface, reduces the errors due to the alterations of surface roughness encountered in many other polymers. It can be homogeneously doped with organic and inorganic compounds in the prepolymer state or solution dipping of the cured pieces. In this study, PDMS pieces are prepared and doped with organic compounds and their CTCs (Part A) and inorganic nanocrystals (Part B). Additionally, undoped samples were prepared under the same conditions as controls. The details of sample preparation are discussed in the Sample Preparation sections of Part A and Part B.

**Polymer beads for experiments in solutions.** Polytetrafluoroethylene (PTFE) beads of diameter 1.6 mm were used in the charging and discharging experiments of the polymers in contact with the CTC or QD solutions. PTFE was used in previous studies for similar experiments and provided a chemically inert, easily contact-charging surface. It is not hydrophilic, and the results of the experiments are not prone to subtle changes in relative humidity.

## 2.2 Measurement of the Generated Contact Charges

**Tapping setup.** A typical measurement method for the contact charges generated on polymers involves a tapping device [58]. This device provides the data in the form of an electrical potential (in V) rather than directly measuring the charges (in Coulombs). In this thesis, the charging behavior of the doped and undoped PDMS samples was monitored with a noise-free handmade tapping device (**Figure 3.3**). The open circuit electrical potential was obtained by contacting and separating two materials – one of them is the sample, and the other one is a metal. The analyzed sample was attached to the base electrode (a metal), and an aluminum stub was connected to the second electrode. While one material was stationary, the other moved periodically and 'tapped' on the first one. The scheme of this contact and separation cycle is shown in **Figure 2.1.** The cycles were controlled by a microcontroller (Arduino Nano) with components (2N3904 NPN transistor, 1N4007 diode, 1K, and 10K). The tapping frequency of 5 Hz was used to contact-charge polymer pieces in a horizontal mode. The charges generated upon contact and separation are monitored via an oscilloscope. The high-impedance oscilloscope can process the data from the two electrodes independently and has a high resolution for the detection of open-circuit potentials generated in events of contact and separation.

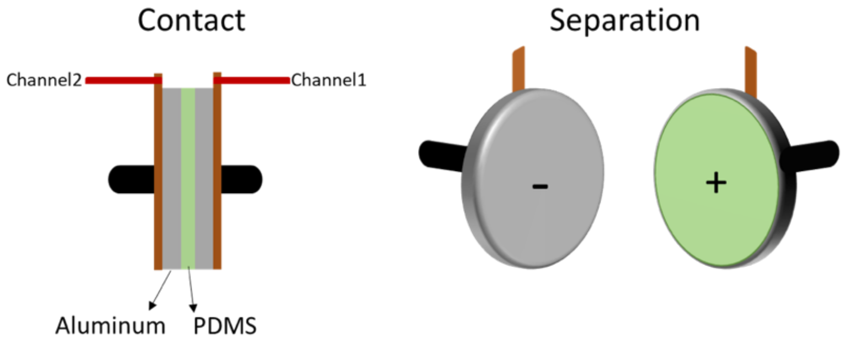

**Figure 2.1**. The scheme tapping setup. The polymer (PDMS) on the metal is attached on one electrode and the Al metal stub is connected to the other electrode.

**Faraday cup measurements.** Undoped, CTCs or QDs doped PDMS polymers were contact charged by touching them to Aluminum foil. Then they were immersed in a Faraday cup (without any contact with the walls or bottom of the cup) attached to an electrometer (Keithley 6517B high precision electrometer). In this setup, the contact charges on the sample pieces induce charge accumulation on the metal Faraday cup, and this charge migration is detected by the attached electrometer (**Figure 2.2**). The charges measured are typically in the range of nano Coulombs (nC) and expressed as the surface charge density (the measured charge divided by the contacted surface area (cm$^2$). In this thesis, we kept all polymers' contact surface area constant therefore we simply reported the charges measured but not the surface charge density.

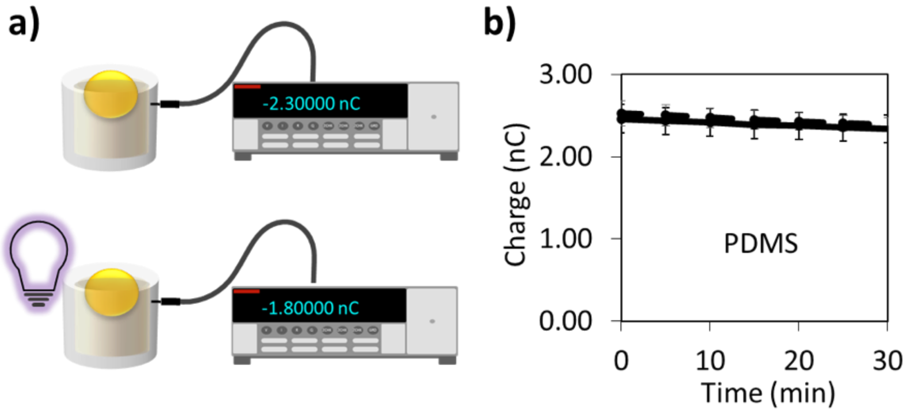

**Figure 2.2**. Contact charge and charge decay measurement setup for solid undoped and doped PDMS pieces. The pieces (shown in yellow in the scheme) are manipulated by tweezers, contact charged against Al foil, and immersed in a Faraday cup. a) The contact charge and charge decay measurements with a homemade Faraday cup attached to an electrometer. b) A typical charge decay plot of PDMS sample in dark (solid line) and under UV illumination (dashed line). The plots overlap since there is no effect of UV illumination on the decay rate of undoped samples. The error bars in the plot display the standard deviation calculated from five independent measurements.

## 2.3 Charge Decay Measurements

We monitored and recorded the dissipation of the contact charges on doped and undoped polymers with two different methods. In the first, CTCs or QDs doped PDMS polymers are contact charged by touching them to Aluminum foil (as shown above), and the contact-charge decay of the samples was examined as a function of time in the solid system. In the second, millimeter-sized solid polymer beads were immersed in a solvent in glass vials and contact-charged by shaking in the vials. A solution of the CTCs or QDs was then added to the vial. In both cases, in solid polymers in the air or the polymer beads in solution, the discharge was further enhanced by using a UV LED lamp with the emission profile shown in **Figure 2.3.**

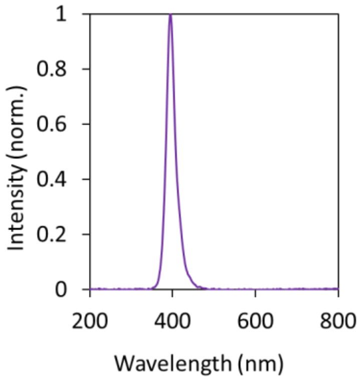

**Figure 2.3**. The emission profile of the UV LED lamp used in the discharge experiments.

### 2.3.1 Charge Decay Measurements of Solid PDMS

The experimental design for charge decay is illustrated in **Figure 2.2a.** All the pieces were first brought into contact several times (until maximum charge, ca. 2.0-2.5 nC) with Aluminum foil for accumulation of contact charges on the surface as described above) Following contact charging, samples were held by tweezers and placed in the homemade Faraday cage. The charges on the polymer pieces were measured by Keithley 6517B high precision electrometer, and their decay was recorded via Kickstart software for at least 20 minutes. The acquired charge and the charge decay measurements were repeated in the dark and under illumination with a UV lamp (9 pieces, 1W in total, emission wavelength maximum, 385-390 nm, as shown in **Figure 2.3**). A typical discharging plot of undoped PDMS is shown in **Figure 2.2b**. The dashed lines indicate the decay plot of PDMS under UV light. Both plots overlap in this figure since UV illumination does not affect the discharge rate of the PDMS.

### 2.3.2 Charge Decay Measurements of Polymer Beads in a Solvent

As mentioned above, polytetrafluoroethylene (PTFE) beads of diameter 1.6 mm were used in the charging and discharging experiments of the polymers in contact with the CTC or

QD solutions. The experiments in a dielectric solvent (hexane) allow us to observe the discharging effect of the additives without involving them directly in the polymer matrix since the additives are added to the system later. In addition to this, since many individual beads are involved in the experiment, higher statistics of the results can be gathered in a shorter time. In each experiment, we first introduced 35 beads in a glass vial with 8 mL (for CTC solution experiments) or 7 mL (for QD solution experiments) in anhydrous hexane. Hexane has a dielectric constant of $\varepsilon$=1.89 at 20°C, which resembles air and serves as a medium for introducing the additive solution. The beads were then mechanically contact-charged using a vortexer for 30 seconds (**Figure 2.4a**). This rotational agitation caused the beads to stick onto the inner wall of the glass vial through electrostatic attraction (**Figure 2.4b**). Using this method, contact-charged beads (each bearing −170 ± 55 pC) retain their charges for many hours to days if they remain unperturbed. Into the vials of contact-charged beads in hexane, CTCs solutions (2.5 µl, 1.0 x $10^{-2}$ M, DCM) or QD solutions (10 µl, 2 mg/mL, hexane) were added using an HPLC syringe (**Figure 2.4c**). Control or comparative discharging experiments were done under the same conditions (RH = 10-40%) by adding the same volume of anhydrous hexane, donor, or acceptor solutions of the same concentration with the CTCs, as described for the specific cases below in the following sections.

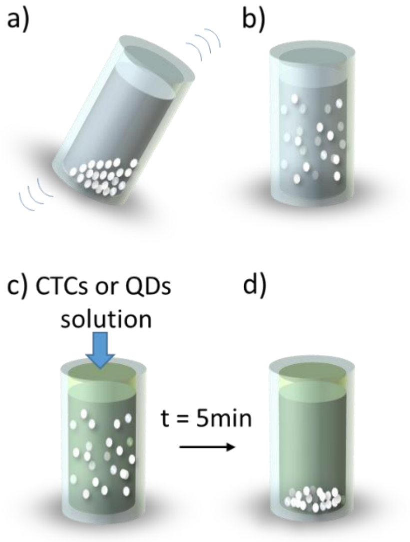

**Figure 2.4**. Schematical representation of the charging and discharging experiments with 35 polytetrafluoroethylene (PTFE) beads in hexane (7 or 8 mL) containing glass vials. a) The beads are mechanically contact-charged using a vortexer for 30 seconds in hexane. b) The contact-charged beads stick to the wall of the glass vial electrostatically. c) Into the vials containing the contact charged beads in hexane, the solution of CTC or QD is dropped by a syringe. d) The beads discharge with the addition of the solutions and drop into the bottom of glass vial with time.

## 2.4 Instrumental Techniques

We used X-Ray Diffraction (XRD), UV-visible Spectroscopy, Fluorescence Spectroscopy, Scanning Electron Microscopy (SEM), Atomic Force Microscopy (AFM), Time-Resolved Fluorescence (TRF), Transmission Electron Microscopy (TEM) accordingly for the characterization of the materials used in this thesis. Also, we used the two-probe method to measure the conductivity of solid samples by an electrometer.

Crystal structures of samples (CTCs and QDs doped PDMS) were analyzed by X-Ray Diffraction. The X'Pert PRO, PANalytical model X-ray diffractometer with Cu Kα radiation was used, and 40 mA current and 45 kV accelerating voltage were applied. The absorption spectra were recorded using a Cary 300 UV–Visible spectrophotometer from Agilent. The surface morphology of samples (CTCs and QDs doped PDMS) was imaged using Thermo Fisher Scientific Quanta 200F model SEM with an accelerating voltage of

15kV. The topography of samples (CTCs doped PDMS) and their surface potential were imaged using a Nanosurf AFM microscope and Kelvin Probe Force Microscopy (KPFM). The emission spectra were obtained using TRF spectroscopy using 2 nm slit widths. PL emission spectra were recorded on TRF spectroscopy using 2 nm slit widths for the excitation and emission. Excitation was set to 390 nm. Time-correlated single photon counting (TCSPC) was used to record luminescence lifetime decays of QD solutions by the same spectrophotometer. A laser diode of 390 nm was used to excite QDs and the emission wavelength was set to their specific emission wavelength maxima. The instrument response function was collected by using 1-2 droplets of LUDOX solution in water to set the α value, which count rates, the percentage of photons coming from the sample.

To understand whether the results in charge formation and dissipation are due to a conductivity change upon doping with the additives, the electrical conductivity of the solid sample (CTC or QD doped PDMS and undoped PDMS) surfaces was measured using the two-probe method. The surface resistivity of the samples was measured using a two-probe method, with w = 17 mm wide samples and the distance between electrodes, d = 217 µm. The resistance values, R, were collected by Keithley electrometer (6517B), which also served as the voltage source using a two-wire resistance measurement setting. 100 V was applied for at least three samples in each group, which gave identical R values. From the resistance measurement, the values were calculated for surface conductivity, ƙ, according to equation ƙ = 1/ρ, ρ= R x (w/d). The mean and the standard deviation of the (thickness independent) surface conductivities were obtained.

## 2.5 Computational Methods

The HOMO and the LUMO energy levels for pristine TCNQ acceptor and pyrene donor with different substitutions were calculated for the optimized geometries using DFT methods with the M06-2X functional [59] and the 6-311G(d) basis set with tight convergence criteria in Gaussian09 [60]. The structures of the individual molecules at the anionic and cationic states were also optimized at the same calculation level to calculate the adiabatic ionization potentials (IP) and electron affinities (EA) using the neutral, anionic, and cationic geometry energies.

The geometries of the binary systems formed by the acceptor and each donor molecule were optimized, and charge transfer values based on the electrostatic potential fitting (ESP) [61] and natural population analysis (NPA) [62] were calculated. The HOMO and LUMO of the binary interactions of charge transfer complex systems were mapped onto the optimized structures. The same process was applied for the quaternary charge transfer complexes; in addition to the HOMO and LUMO, HOMO-1 and LUMO+1 were also mapped onto the optimized quaternary structures. Counterpoise corrected interaction energies between the donor and the acceptor were calculated for the lowest energy structures of the binary and the quaternary complexes. Charge transfer values were also calculated by the method proposed by Kistenmacher et al. [63] using the bond lengths of the optimized individual acceptor molecule and the optimized acceptor molecule in interaction with the donor functionalized with different substituents.

Frontier orbitals were also calculated at the excited state optimized geometry to elucidate the effect of photoexcitation on the electronic structure of these charge transfer cocrystals. Natural transition orbitals from S0→S1 levels were determined for both ground state and excited state optimized geometries by the TDDFT method by calculation of the first 40 excited states and their oscillatory frequencies [64].

# PART A

## Chapter 3

## 3. Introduction to Charge Transfer Complexes

The first CT complex, quinhydrone, was reported in 1844 [65]. Since the discovery of the organic metal TTF-TCNQ in 1973, there has been a great interest in organic CTCs [66]. CTCs have non-covalent interactions with definite stoichiometries. Alteration of morphology and crystal packing of CTCs yield different physical and chemical properties of the materials. Organic CTCs have recently attracted attention in organic optoelectronic applications (optoelectronic devices), the pharmaceutical industry, and static electricity applications (electrophotography) [67], [68], [69], [70], [71]. This chapter gives general information on the preparation, crystal structure, characterization, degree of charge transfer, and electronic properties of CTCs. We also present the aim of using CTCs as antistatic additives in polymers.

### 3.1 Donors and Acceptors

Organic charge transfer complexes (CTC) have unique features which are different from their precursors, π-donors (D) and π-acceptors (A). As the name implies, an electron is transferred from the donor (D) to the acceptor (A) in a CTC. During this transfer, it is plausible to state that the electron from the donor's highest occupied molecular orbital (HOMO) is transferred to the lowest unoccupied molecular orbital (LUMO) of the acceptor. **Figure 3.1a** shows the respective energy levels of the frontier orbitals of a donor and an acceptor and the charge transfer. The formed charge transfer complex ($D^+$-$A^-$) has a decreased HOMO-LUMO energy gap compared to the donor and acceptor. The complexes usually have vivid colors different than those of donors and acceptors, which is evidence of the HOMO-LUMO gap decrease, which makes the CTC absorb in the visible region of the spectrum. This gap is further decreased upon excitation of the complex (**Figure 3.1b**) [7].

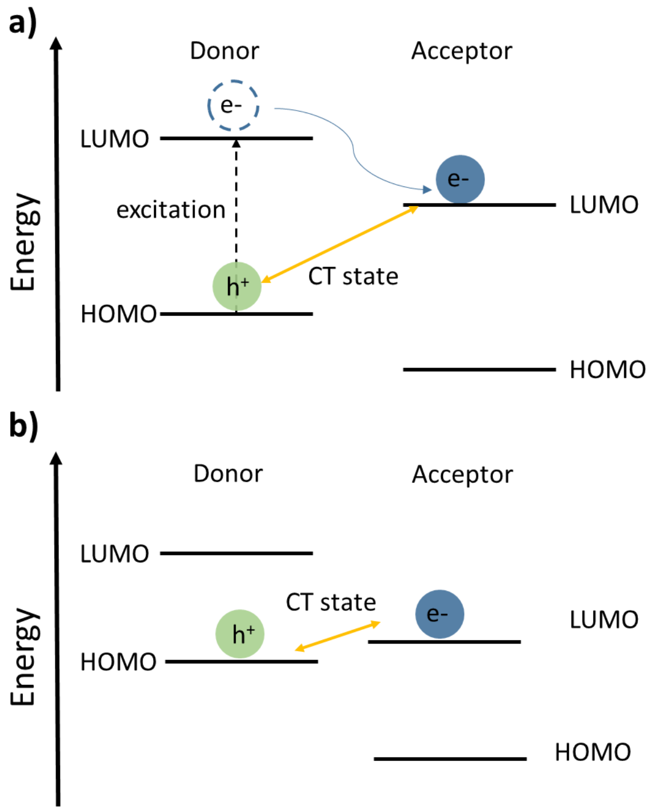

**Figure 3.1.** Respective energy levels of donor and acceptor frontier orbitals, and the charge transfer state. a) ground-state CT interaction. b) excited-state CT interaction facilitated by a lower HOMO-LUMO gap.

For CTCs, an acceptor with high electron affinity and a donor with low ionization energy make ideal pairs. Tetracyanoquinodimethane, TCNQ, and Tetracyanoethylene, TCNE, which have high electron affinities, are strong electron acceptor molecules. In their donor-acceptor complexes, these molecules form radical anions ($\mathrm{TCNQ}^{\cdot-}$ and $\mathrm{TCNE}^{\cdot}$). TCNQ, our choice of acceptor in this study, has been one of the most studied acceptor molecules since its first synthesis in 1962 [72]. It has a central hexagonal ring, which is aromatized when taking an electron, and four low-lying, vacant C≡N $\pi^*$-orbitals, which can help to accommodate and delocalize the incoming electron [73]. Planar molecules enhance the charge transfer in CTCs – delocalizing the formed charge - but it is not a strict condition, e.g., in fullerene [74]. The delocalization logic holds for good donors, too: Polyaromatic hydrocarbons, such as pyrene, naphthalene, anthracene, tetracene, and pentacene, have high levels of conjugation, making them good electron donors when they make a complex with TCNQ [75]. Some examples of common donors and acceptors in organic CTCs are shown in **Table 3.1**.

**Table 3.1**. Common examples of donor and acceptor molecules used in cocrystals.

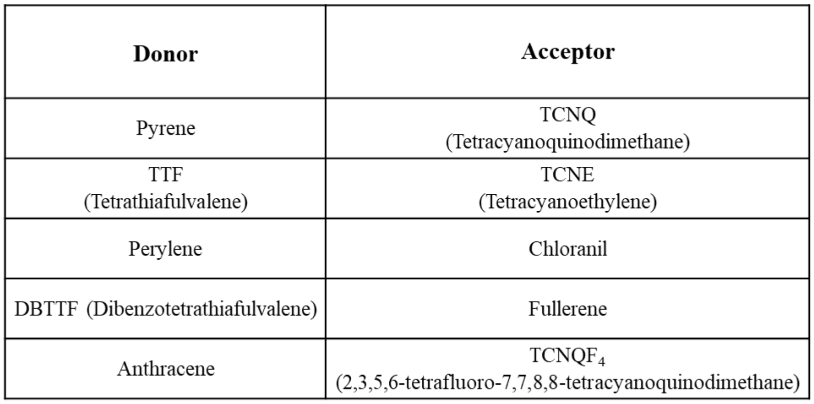

| **Donor** | **Acceptor** |
|---|---|
| Pyrene | TCNQ<br>(Tetracyanoquinodimethane) |
| TTF<br>(Tetrathiafulvalene) | TCNE<br>(Tetracyanoethylene) |
| Perylene | Chloranil |
| DBTTF (Dibenzotetrathiafulvalene) | Fullerene |
| Anthracene | $TCNQF_4$<br>(2,3,5,6-tetrafluoro-7,7,8,8-tetracyanoquinodimethane) |

## 3.2 Crystal Structure

CTCs can form in different stoichiometries, 1:1, 2:1, 3:1, and 3:2. However, the 1:1 complex ratio is the most common crystal structure [76]. CTCs usually have two different crystal structures, mixed and segregated. The two stacking geometries are shown in **Figure 3.2.** The stacking formation, mixed-stack (-DADADA) or segregated (-DDD-AAA) arrangement, impacts the physicochemical properties of the CTCs. The crystal structure and the differences resulting from the different stacking geometries can be analyzed using XRD, UV-vis, IR spectroscopy, Raman spectroscopy, and conductivity measurements. Mixed-stack crystals generally are insulators with face-to-face interactions; hence semiconductor CTCs with the mixed-stack arrangement are rare exceptions. On the other hand, CTCs with segregated stacking show metallic properties [77]. The tilt angle between the donor and acceptor changes the degree of charge transfer and electrical conductivity. If $0.5 < q < 0.74$, the complex usually exhibits metallic behavior having a segregated structure [78]. At the same time, a better overlap of the donor and acceptor frontier orbitals is associated with a higher degree of charge transfer [76]. Understanding the formation mechanism of these complexes is crucial to designing CTCs and optimizing their functions.

Anthracene-TCNQ, Pyrene-TCNQ, Perylene-TCNQ, and DBTTF-TCNQ CTCs have mixed stacking arrangements with 1:1 stoichiometry [77]. TTF-TCNQ, a common charge transfer salt, has segregated stacking [78]. TMTSF-TCNQ may have both the stacking geometries [77].

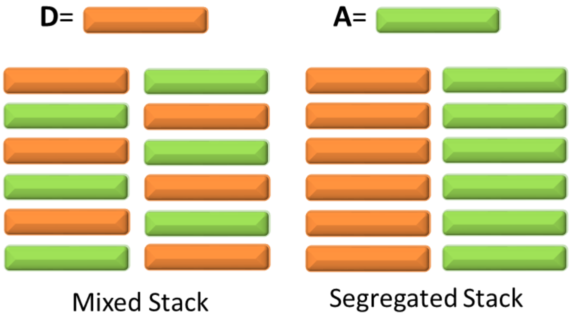

**Figure 3.2**. Mixed and segregated stacking structures of donors and acceptors in CT cocrystals of 1:1 donor/acceptor ratio.

## 3.3 The degree of Charge Transfer and the Electronic Properties

The electronic coupling between the donor and the acceptor generates a degree of charge transfer (ρ), which affects the material's conductivity. The difference in the ionization potential of the donor ($I_D$) and the acceptor's electron affinity ($E_A$) is related to the degree of charge transfer. The degree of charge transfer affects the tilt angle and bond length along the stacks of the electron donating-accepting moieties. The degree of charge transfer (ρ) in the CTCs complexes, for example, those of TCNQ with different donors, can be predicted using the bond length changes in the acceptor. More precisely, the population of the electron in LUMO changes the lengths of the TCNQ bonds, which can be followed by the changes in their vibration frequencies in Raman or IR spectra [79]. The structure of TCNQ is shown in **Figure 3.3**.

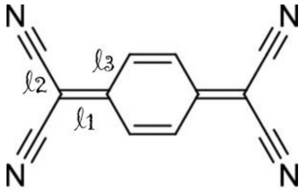

**Figure 3.3.** The structure of TCNQ indicating bond lengths.

In our CTC experiments, we chose TCNQ as the acceptor and pyrene and its derivatives as the donor for the formation of the CTCs. Kistenmacher method can be used to calculate the degree of charge transfer in such CTCs, using the change in the TCNQ bond lengths: [63].

$$\boldsymbol{\alpha_i = \frac{\ell_1}{\ell_2 + \ell_3}}$$

$$\boldsymbol{\rho = -\frac{\alpha_{CT} - \alpha_0}{\alpha_{-1} - \alpha_0}}$$

Where $\ell$ is the bond length described in **Figure 3.3** and subscript i = 0, −1, CT: denotes the neutral molecule, the anion, and the complex, respectively. The stability of the complex is attained by the non-covalent interactions of D/A pairs (TCNQ and polycyclic aromatic hydrocarbons), such as the π-π interactions leading to CT, hydrogen bonding, and van der Waals interactions [80]. It was found that the hydrogen bonds dictate the charge carrier polarity of charge transfer complexes with TCNQ, and halogen bonds affect the degree of charge transfer and the neutral to ionic transitions.

## 3.4 Our aim of using CTCs as Additives for Discharging of Contact-charges on Polymers

In 2019, our group published a report on dissipating contact charges on common polymers remotely by light [51]. This first example of remote control of contact charges involved the inclusion of some organic dye molecules in the polymer matrices. The organic dyes in the ground state did not yield to a discharge of the charges on the polymers that they reside in, but when they were excited by the proper wavelength of light, the charges quickly dissipated. It was then hypothesized that the higher dipole moments and the (minute amounts of) charge separation led to this discharging effect of the excited dyes. However, in this study, a tendency for higher dipole moments was the hint to discharge. Still, a deeper understanding of the discharge mechanism was impossible since the dyes were of different chemical structures.

In this thesis work, we aim to form a set of CTCs as antistatic additives in polymers. The purpose is to extend the understanding of the discharge mechanism of the contact charges with the additions and excitations of the organic molecules in polymers. We slightly changed the target from single molecules to their CTCs, since CTCs have an inherent ‘dipole moment’ because of the CT process upon their formation. In addition, this dipole moment can be increased upon excitation, as reported in the literature. Also, for most CTCs, it was shown that known computational methods could calculate the degree of charge transfer. These facts, together with the opportunity of having a set of CTCs with slightly different chemical structures, may help to assess the effect of chemical structural changes in the additive CTC on its discharging performance. Finally, a mechanism of discharge mediated with CTC (without or with light) can be proposed.

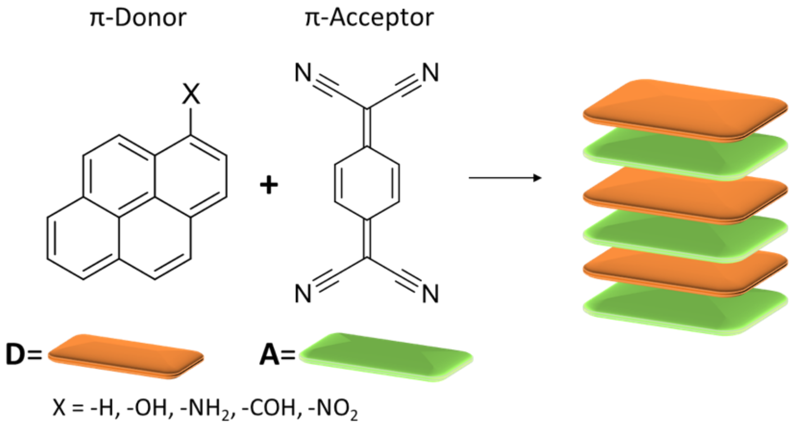

**Figure 3.4.** Mixed stack structure of the CTCs formed by the pyrene derivatives and TCNQ

The chosen set should be an insulator CTC family that is synthetically easily accessible and low cost, with background literature on CT efficiency. Matching these criteria, we chose TCNQ as our acceptor, and as donors, we chose pyrene and its derivatives 1-aminopyrene, 1-hydroxypyrene, 1-pyrenecarboxaldehyde, 1-nitropyrene. All of the CTCs formed are in the mixed stack structure and are insulators. The different chemical groups on the pyrene ring provide slight changes in the electronic structures of the CTC formed. For example, the literature shows that the HOMO of 1-Aminopyrene has a lower energy gap with the LUMO of the TCNQ than that of pyrene. This decrease is due to the resonance effect of -NH$_2$ and the existence of hydrogen bonding with TCNQ.

For the triboelectric discharging experiments, the CTC donor and acceptors shall not have a discharging effect individually to mark the difference that would be affected by the CTC. In our previous study, pyrene and its derivatives have shown this inactivity (also upon excitation with light). As also displayed below, TCNQ can help discharge the solid polymer it is doped in with rates slightly faster than the undoped one. However, this discharge is not further enhanced by light.

For all these reasons, the discharging of polymers with CTCs additives and our choices of materials stand as a reasonable next step in the field of electrostatic research.

## Chapter 4

# 4. Control of Contact Charging of Polymers with Charge Transfer Complexes

In this chapter, we describe the preparation of the CTCs, the preparation of the PDMS samples, the doping method for CTCs into the PDMS, and the characterization of CTCs and the doped polymers. Finally, we display the results of charging/discharging experiments with CTC-doped PDMS and CTC discharging of the polymers charged in the solution.

## 4.1 Experimental

### 4.1.1 Formation of the Charge Transfer Complexes in Solution

Pyrene derivatives and TCNQ were dissolved in dichloromethane in different vials to have $1.0 \times 10^{-2}$ M solutions. CTCs solutions were prepared by mixing the two solutions at room temperature. Upon mixing, the color of the solution changed due to the formation of the charge transfer band (See **Figure 4.1** for the change in the color upon formation of the CTC complex with pyrene and TCNQ). UV-Vis spectra of the CTCs reveal the spectral changes and the emergence of the CT band (**Figures 4.2a and b**). The formation of the complexes can also be followed by XRD patterns of the CTCs (in PDMS). Two examples of such diffractograms are given in **Figure 4.2c**.

The prepared solutions are used in doping the solid PDMS pieces as described next (Section 4.1.2) and in the discharging of the PTFE beads in solution (Section 4.2.2).

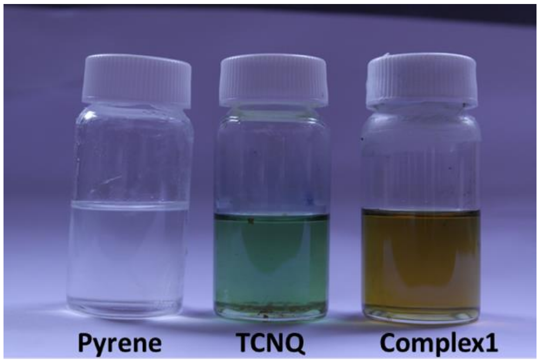

**Figure 4.1.** The photos of the dichloromethane solutions of pyrene, TCNQ, and their CTC (Complex 1), each solution is 1.0 x $10^{-2}$ M. Note the deeper color of the CTC compared to the other solutions (because of the existence of the charge transfer band).

**Table 4.1**. The naming of the different CTCs formed with the given derivatives of pyrene as donors and TCNQ as the acceptor.

| **Code** | **Donor** | **Acceptor** |
|---|---|---|
| Complex1 | Pyrene | TCNQ |
| Complex2 | 1-Aminopyrene | TCNQ |
| Complex3 | 1-Pyrenecarboxaldehyde | TCNQ |
| Complex4 | 1-Hydroxypyrene | TCNQ |
| Complex5 | 1-Nitropyrene | TCNQ |

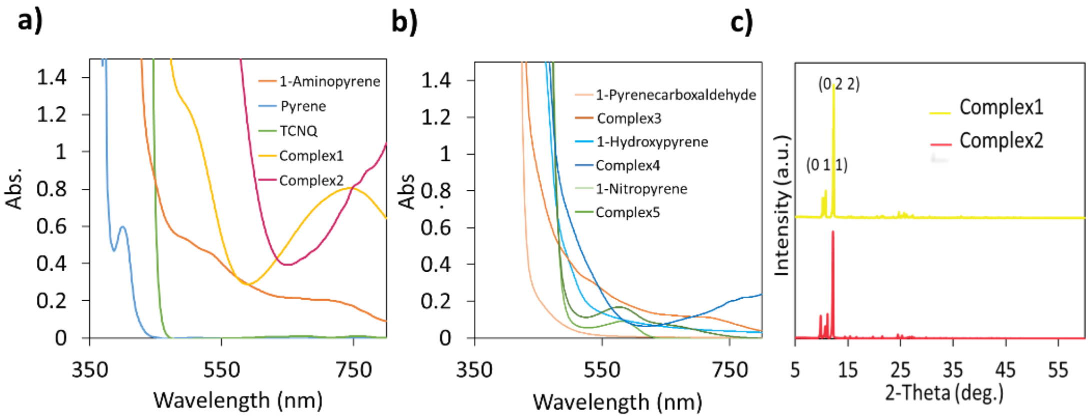

**Figure 4.2.** a) UV-visible spectra of CTCs, the acceptors and donors in dichloromethane (1.0 x $10^{-2}$ M). Complex1 (yellow), Complex2 (pink), 1-Aminopyrene (orange), TCNQ (green), Pyrene (blue). b) UV-visible spectra of CTCs with donors in dichloromethane (1.0 x $10^{-2}$ M) – 1-pyrenecarboxaldehyde (light orange), Complex3 (dark orange), 1-nitropyrene (light green), Complex5 (dark green), 1-Hydroxypyrene (light blue), and Complex4 (dark blue). The broad bands indicate the charge transfer bands compared to donors. c) The X-ray diffractograms of pyrene-TCNQ and 1-Aminopyrene-TCNQ.

### 4.1.2 Preparation of the Charge Transfer Complexes doped PDMS

To prepare the PDMS samples, the components of the PDMS kit (Dow chemicals, Sylgard 184), the base polymer, and the curing agent of PDMS were mixed in a 10:1 ratio [81]. The prepolymer mixture was put under vacuum for degassing to remove $H_2$ (g) formed during the polymerization reaction and the bubbles forming during the mixing. Then, the prepolymer was poured into the polystyrene dishes, and the dishes were left in an oven for 24 hours at 70°C for complete curing. The formed elastomer PDMS was cut into (0.9 cm radius, 1.52 mm thickness) pieces. They were washed with dichloromethane for 24 hours in a vial to remove unreacted reagents and the catalyst. Then, the pieces were dried overnight.

Dried PDMS pieces were then immersed in vials with the donor, acceptor, and CTC solutions (1.0 x $10^{-2}$ M, 30 mL) for 24 h. Undoped pieces were also maintained under the same conditions in dichloromethane to be served as control samples. The solvent-swollen samples are left to dry slowly one day before the experiments. For one experiment to test the effect of the concentration, a sample of PDMS was let in another concentration (1.0 x

$10^{-3}$ M) of Complex 2. Two examples of the UV-vis spectra of the CTC-doped PDMS samples are shown in **Figure 4.3**.

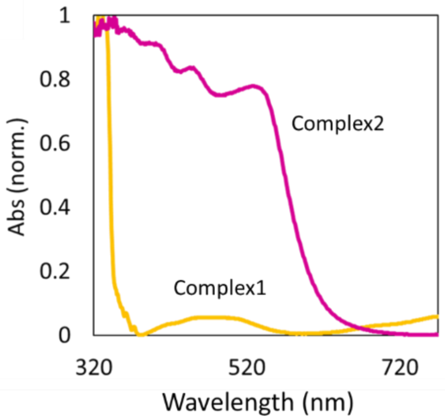

**Figure 4.3**. a) Solid state UV-visible spectra of pyrene-TCNQ (yellow) and 1-Aminopyrene-TCNQ (pink).

## 4.2 Charging Experiments of CTCs in Solid System

As described in **Figure 2.1** (Section 2.2 Measurement of the Generated Contact Charges), a tapping setup establishes contact/separate cycles of PDMS and the Al metal. These cycles led to contact charging of both materials, and the formed could be measured and recorded as open circuit potential by a high-impedance oscilloscope. The difference in the open circuit potentials obtained in such contact/separation cycles between the identically tapped Complex2-doped, Complex1-doped PDMS, and undoped PDMS can be visualized in **Figure 4.9**. The $V_{oc}$ obtained by the Complex 2-doped PDMS is one-tenth that of the undoped PDMS, displaying the antistatic action of the CTC doping. All CTC-doped PDMS samples showed antistatic behavior; the obtained decrease in $V_{oc}$ depends on the type of CTC used.

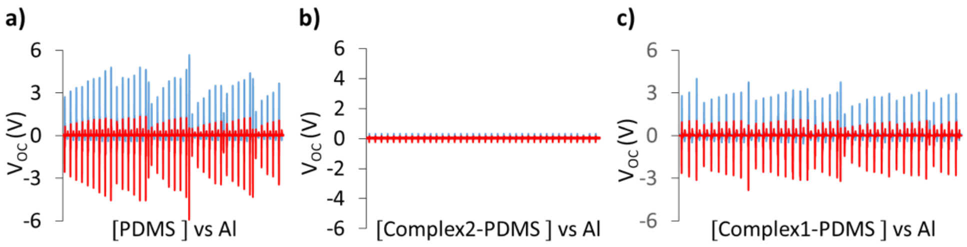

**Figure 4.4.** a) Open circuit ($V_{oc}$) signals obtained from aluminum electrode (red) that is tapped to the undoped PDMS and from the metal electrode (blue) placed behind polymer surface (18 mm diameter, 1.0 mm thick). b) Under same conditions and with the same setup b) $V_{oc}$ signals from Complex2 doped PDMS surface and aluminum electrode both decrease to one-tenth of those obtained by undoped PDMS, and c) $V_{oc}$ signals from Complex 1 doped PDMS surface and aluminum electrode show that the decrease in the $V_{oc}$ is depending on the type of the CTC used. For the tapping setup details see Section 2.2, and **Figure 2.1**.

## 4.3 Charge Decay Experiments

### 4.3.1 Charge Decay Experiments of CTC-doped PDMS

Undoped PDMS and PDMS pieces doped with TCNQ, pyrene, 1-aminopyrene, and their CTCs were brought into contact with aluminum foil until they reached -2.5 nC by holding and tapping them with tweezers on the foil. After the contact charging, they were placed into a homemade Faraday cage attached to a high-precision electrometer (**Figure 2.2**) (Section 2.3.1, Charge Decay Measurements in Solid System (PDMS)). The surface potential was recorded under dark and UV illumination with respect to time (**Figure 4.5**). As analyzed by fitting first order and second order decay rate equations on the experimental decay profiles, on the pyrene, TCNQ, 1-aminopyrene, Complex1, and Complex2 doped PDMS samples charges decay according to the first order kinetics in the dark and 30 mins of illumination whereas on Complex2 the decay fits the second order in dark and UV illumination in five minutes. The calculated decay rates are shown in **Table 4.2**.

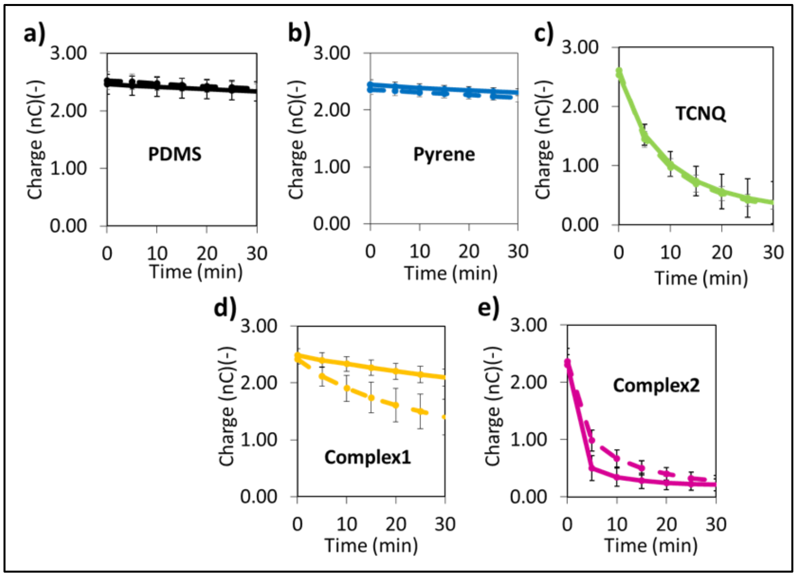

**Figure 4.5.** The discharge of contact-charges on PDMS doped with CTCs, in dark (lines) and under UV illumination (dashed lines). On CTC-doped PDMS, contact charges decay faster than the undoped ones of the ones doped only with the donor. Illumination makes a difference in the charge decay for the polymers doped with CTC. For the preparation details of the samples see Section 4.1.2. Error bars denote the standard deviations from at least four independent measurements. (RH = 40-55%).

**Table 4.2** The charging decay rate of samples are fitted in first order kinetic (30 min). *= The discharging curve is fitted in second order kinetic (5 min).

| | **Mean ± SD** |
|---|---|
| **Sample** | **Rate Constant ($s^{-1}$)** |
| PDMS Dark | 0.002 ± 0.001 |
| PDMS UV | 0.002 ± 0.001 |
| Pyrene Dark | 0.002 ± 0.000 |
| Pyrene UV | 0.002 ± 0.001 |
| 1-Aminopyrene Dark | 0.006 ± 0.002 |
| 1-Aminopyrene UV | 0.024 ± 0.008 |
| TCNQ Dark | 0.061 ± 0.022 |
| TCNQ UV | 0.063 ± 0.006 |
| Complex1 Dark | 0.006 ± 0.001 |
| Complex1 UV | 0.014 ± 0.006 |
| Complex2 Dark* | 0.349 ± 0.143 |
| Complex2 UV* | 0.115 ± 0.028 |

Complex 2 was also used in understanding the effect of CTC doping concentration on the discharge rate of the charged samples. The charge decay on PDMS, Complex2 (1.0 x10$^{-3}$), and Complex2 (1.0 x10$^{-3}$) obey first-order kinetics in dark with 0.0123 s$^{-1}$, 0.0108 s$^{-1}$, and 0.0746 s$^{-1}$, respectively. In the presence of UV, these decay rates became 0.0134 s$^{-1}$, 0.0157 s$^{-1}$, and 0.0493 s$^{-1}$. We observed that the discharge rate when the concentration of the complex increases.

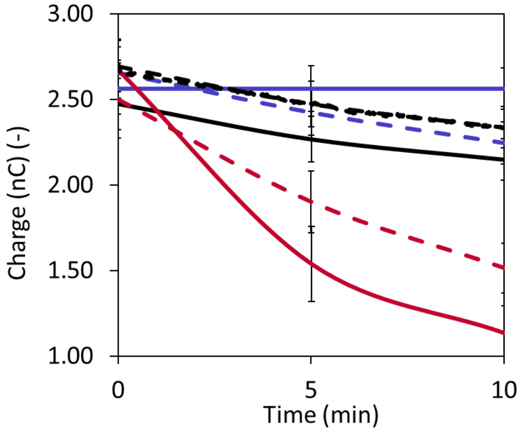

**Figure 4.6.** The discharging of contact charges on undoped PDMS (black), Complex 2 (1.0 x 10$^{-3}$ M, purple), and Complex 2 (1.0 x 10$^{-2}$ M, pink) with time. For the preparation details of the samples see Section 4.1.2. Error bars denote the standard deviations from at least four independent measurements. (RH = 15-30%).

The surface conductivities of CTCs doped and undoped PDMS samples were measured and lie in the insulator range (**Table 4.3**), as expected. The illumination did not affect the surface conductivity values, either. These values showed that the charge dissipation was not caused by an overall increase in the surface conductivity of the composites.

**Table 4.3.** The surface conductivity of PDMS samples doped with the donor, acceptor, and the complexes measured in dark and under UV. For the preparation of the samples and the details on the conductivity measurement, see Sections 4.1.2 and 2.3. Error bars denote the standard deviations from at least four independent measurements.

| **Material** | **Conductivity (S)** |
|---|---|
| PDMS Dark | $9.45 \text{ x } 10^{-14}$ |
| PDMS UV | $9.44 \text{ x } 10^{-14}$ |
| Pyrene Dark | $8.86 \text{ x } 10^{-14}$ |
| Pyrene UV | $8.82 \text{ x } 10^{-14}$ |
| Aminopyrene Dark | $8.33 \text{ x } 10^{-14}$ |
| Aminopyrene UV | $8.33 \text{ x } 10^{-14}$ |
| TCNQ Dark | $7.82 \text{ x } 10^{-14}$ |
| TCNQ UV | $7.67 \text{ x } 10^{-14}$ |
| Complex1 Dark | $5.39 \text{ x } 10^{-14}$ |
| Complex1 UV | $5.37 \text{ x } 10^{-14}$ |
| Complex2 Dark | $5.55 \text{ x } 10^{-14}$ |
| Complex2 UV | $5.55 \text{ x } 10^{-14}$ |

### 4.3.2 Charge Decay Experiments with Polymers in contact with CTC Solution

As described in **Figure 2.4** (Section 2.3.2 Charge Decay Measurements of Polymer Beads in a Solvent), 35 PTFE beads were introduced in glass vials with 8 mL hexane. Then the beads were mechanically contact-charged using a vortexer for 30 seconds which is demonstrated. After vortexer charging, a 2.5 µl solution of CTCs (Complex1, Complex2, donors, or acceptor ($1.0 \text{ x } 10^{-2}$ M, dichloromethane) were introduced into the hexane with contact-charged beads. No bead discharged when we added only dichloromethane or the solutions of only pyrene and its derivatives. However, after additions of the CTCs, the beads discharged quickly. A comparison of the discharging of beads in the solutions of a donor and its CTC over time for the first five minutes after the solutions were added is shown in **Figure 4.7.** The numbers of discharging beads five minutes after the addition of each of the CTC solutions are shown in **Figure 4.8.**

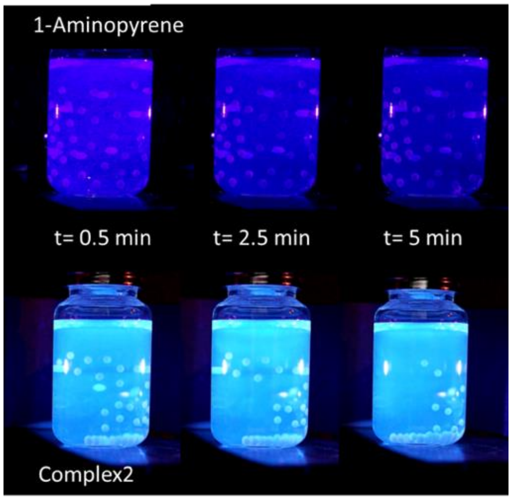

**Figure 4.7.** A comparison of the discharging of beads over time, in the solutions (1.0 x $10^{-2}$ M, dichloromethane) of 1-aminopyrene, and Complex 2 (1-aminopyrene/TCNQ) introduced into charged beads in hexane (8 mL) in glass vials. In the first five minutes the difference is clear: With the CTC solution, the beads discharge faster. For a more quantitative look, see **Figure 4.8**.

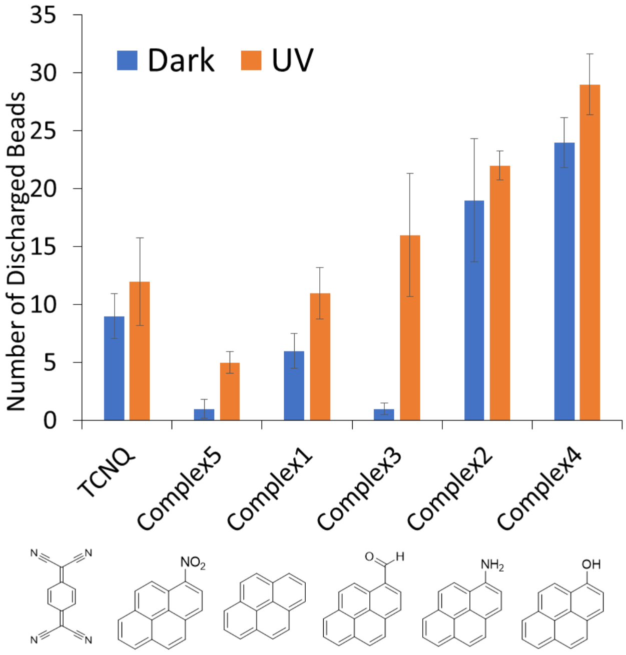

**Figure 4.8:** The number of discharging beads in hexane (8 mL) in glass vials, five minutes after the addition of TCNQ solution and each of the CTC solutions (1.0 x $10^{-2}$ M, dichloromethane) with the donor shown. (RH = 40-55 %).

## 4.4 Discussion

### 4.4.1 The Effect of HOMO-LUMO Gap in the Charge Dissipation in Polymers

As shown in the charging and discharging experiments, the complexes formed by pyrene derivatives with TCNQ displayed antistatic activity and faster discharging compared to the undoped PDMS. However, some CTCs of some pyrene derivatives were faster in discharging than others. We propose that these differences are due to the differences in the energy levels in the CTCs formed with different derivatives, giving rise to varying amounts of charge transfer within the complex. This difference leads to different propensities of discharge ability. To understand these differences and the charge transfer between the acceptor and substituted donor derivatives, first, the geometries of the single molecule structures (TCNQ, pyrene, and its derivatives) were optimized, and ground state energy levels were determined. Various pairwise complex geometries were constructed by varying intermolecular distance and orientation and were subjected to geometry optimization to determine the lowest energy structures for the binary complex. According to the results obtained, it was concluded that the minimum energy pairwise geometries are formed by the π-stacking of the donor and acceptor molecules, as expected (**Figure 4.9**). This π-stacked structure model was used to construct initial guesses for quadruple charge transfer complex geometries. Next, the HOMO and LUMO energy levels of the optimized pristine donor and acceptor structures were calculated (**Figure 4.10a**). For all binary and quaternary complexes, The HOMO and LUMO of the pairwise CTCs structures demonstrated that the HOMOs of all the pairwise CTCs are on the donor molecules and the LUMOs are on the acceptor molecule (**Figures 4.9 and 4.10**). HOMO-1 orbitals are on the donor, and LUMO+1 orbitals are on the acceptor for the quaternary complex (**Figure 4.10b**). Two donor molecules in quadruple CTCs bear HOMO and HOMO-1 on them, while the two acceptor molecules bear LUMO and LUMO+1. Similar trends for frontier orbital energies and their distributions were observed using B3LYP-D3 and wB97XD functionals.

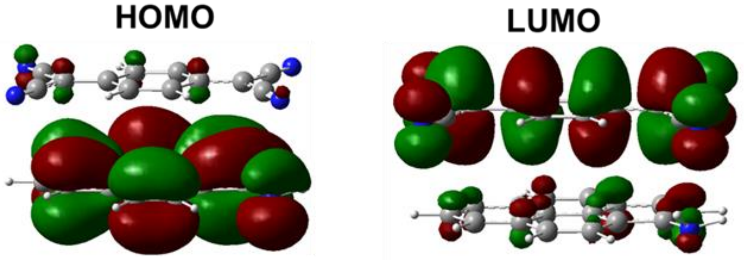

**Figure 4.9.** HOMO and LUMO orbitals mapped on the pairwise interactions of donor-acceptor charge transfer complex for -$NH_2$ substitutions on pyrene donor.

The calculated energy levels (**Figure 4.10**) show that the CTCs leading to more efficient or faster discharging formed from the donors with the higher lying HOMOs and hence with the smallest HOMO donor-LUMO acceptor gap. For example, according to all DFT calculations with different functionals, the LUMO of the acceptor TCNQ is the closest to the HOMO of the pyrene donor with -$NH_2$ and -OH substitution. These CTCs show the best performance for charge dissipation among all CTCs studied (**Figure 4.8**).

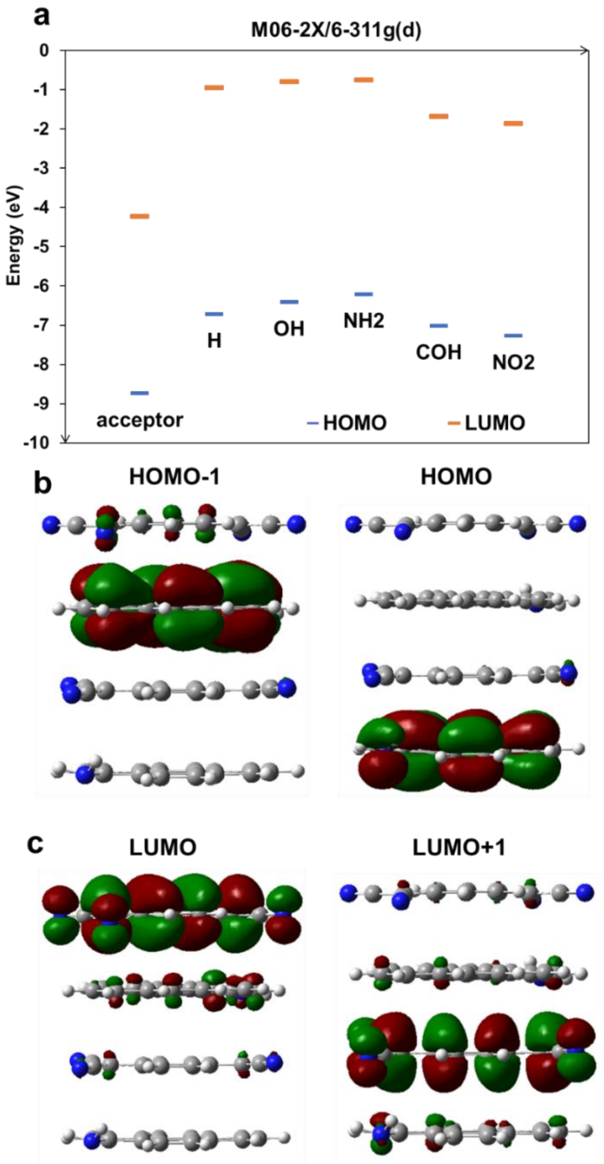

**Figure 4.10.** a) HOMO and LUMO energy levels for the acceptor and the donor with different substitutions, b) HOMO and HOMO-1 orbitals, c) LUMO and LUMO+1 orbitals mapped on the quadruple interactions of donor-acceptor charge transfer complex for -$NH_2$ substitutions on pyrene donor.

### 4.4.2 The Relation between Degree of Charge Transfer and Triboelectrification

Charge transfer values showing the degree of the charge transfer between the donor and acceptor can be compared and expressed in different ways. In the first way, the ionization potential of the donor and the electron affinity of the acceptor is handled. The adiabatic ionization potential values for the donor molecules (**Table 4.4**) were obtained by taking the difference between the energy of the optimized positively charged molecule and the energy of the optimized neutral molecule. For the acceptor molecule, the adiabatic electron affinity (**Tables 4.4 and 4.5**) was calculated by taking the difference between the energy of the optimized negatively charged TCNQ and the energy of the optimized neutral TCNQ. For enhanced charge transfer, it was already known that the HOMO energy of the donor should be close to the LUMO energy of the acceptor and that the donor should have a lower ionization potential [82]. Considering **Table 4.5**, the best charge transfer values in CTCs can be achieved using a donor molecule with a lower ionization potential. We found that the smaller the IP of the donor, the more effective the charge transfer as calculated lowest for with amine and hydroxy substitutions of pyrene donor. Pyrenes with these substitutions also have the least negative EA values. Considering the HOMO energy levels and ionization potentials among donor molecules, 1-aminopyrene and 1-hydroxypyrene have the best values as donors in CTCs. Furthermore, the change in dipole moment $|\Delta\mu|$ is associated with the electronic coupling factor and electron transfer [83]. The electron coupling is a focal factor for the degree of charge transfer ($\rho$) [77].

**Table 4.4.** The effect of donor substitution on the charge transfer values, IP and EA differences and interaction energies between donor and acceptor for pairwise and quadruple interactions (CTCs).

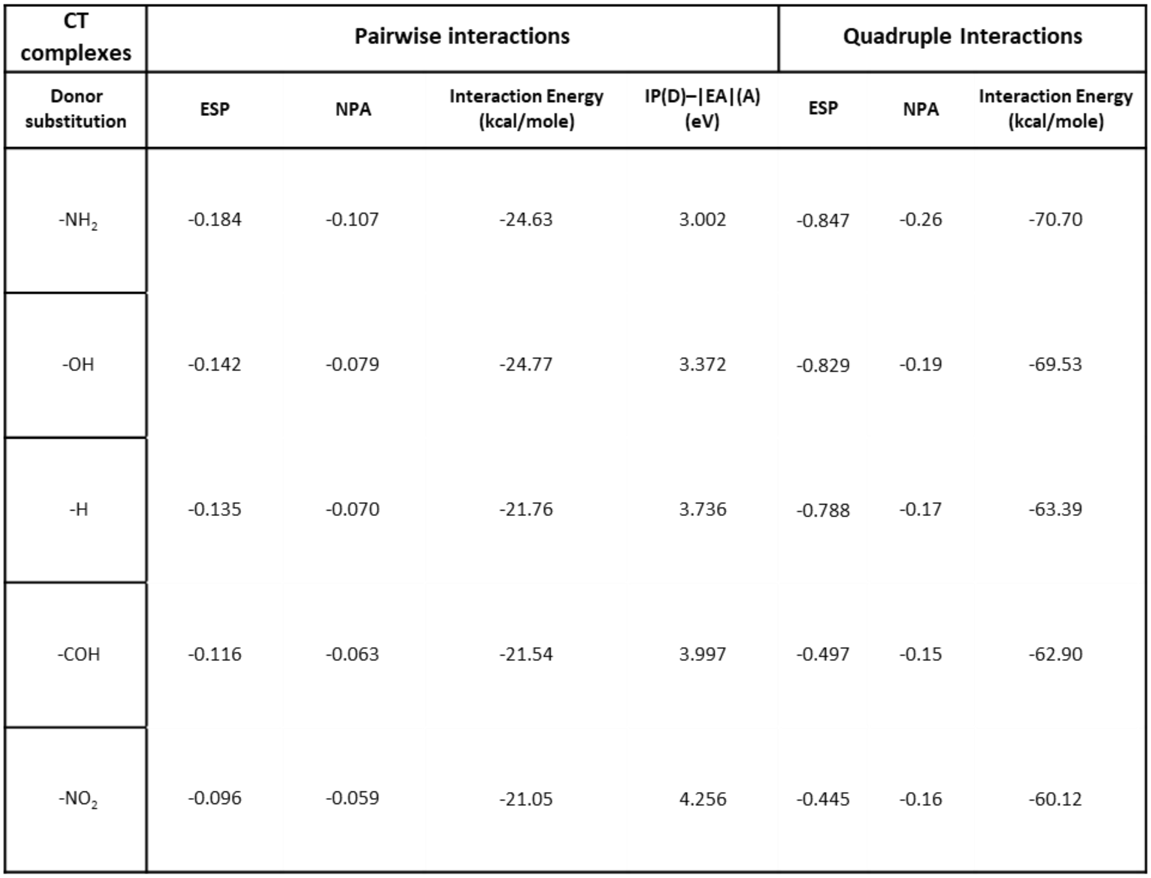

| CT complexes | Pairwise interactions | | | | Quadruple Interactions | | |
|---|---|---|---|---|---|---|---|
| **Donor substitution** | **ESP** | **NPA** | **Interaction Energy (kcal/mole)** | **IP(D)–\|EA\|(A) (eV)** | **ESP** | **NPA** | **Interaction Energy (kcal/mole)** |
| $-NH_2$ | -0.184 | -0.107 | -24.63 | 3.002 | -0.847 | -0.26 | -70.70 |
| -OH | -0.142 | -0.079 | -24.77 | 3.372 | -0.829 | -0.19 | -69.53 |
| -H | -0.135 | -0.070 | -21.76 | 3.736 | -0.788 | -0.17 | -63.39 |
| -COH | -0.116 | -0.063 | -21.54 | 3.997 | -0.497 | -0.15 | -62.90 |
| $-NO_2$ | -0.096 | -0.059 | -21.05 | 4.256 | -0.445 | -0.16 | -60.12 |

**Table 4.5.** Electron affinity and ionization potentials of the donors and the acceptor used in this work. EA values calculated at the M062x/6-311g(D) level by taking the energy difference of the optimized anion structure and the optimized neutral structure. IP values calculated at the M062x/6-311g(d) level by taking the energy difference of the optimized cation structure and the optimized neutral structure

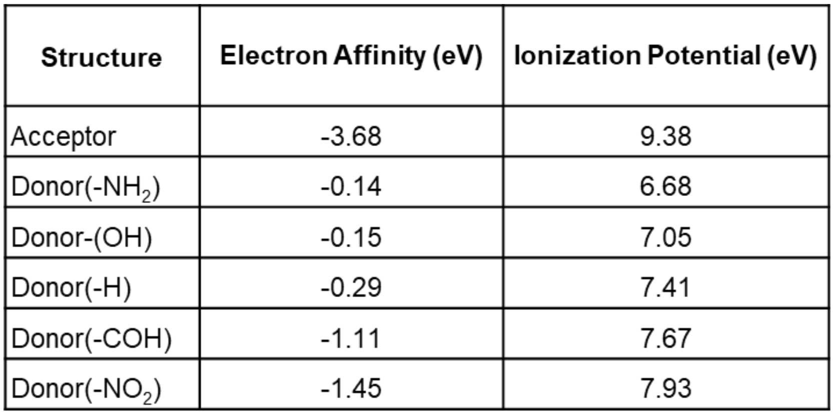

| Structure | Electron Affinity (eV) | Ionization Potential (eV) |
|---|---|---|
| Acceptor | -3.68 | 9.38 |
| Donor(-$NH_2$) | -0.14 | 6.68 |
| Donor-(OH) | -0.15 | 7.05 |
| Donor(-H) | -0.29 | 7.41 |
| Donor(-COH) | -1.11 | 7.67 |
| Donor(-$NO_2$) | -1.45 | 7.93 |

In the other three methods, pairwise and quadruple stacks of the donor and acceptor are considered. The charge transfer values for these stacks were obtained by the ground state electrostatic potential (ESP) and natural population analysis (NPA) (**Table 4.4**), resulting in the same trends. The interaction energies for pairwise and quadruple structures are given in **Table 4.4**, which indicates that the interaction energies between donor and acceptor in Complex 2 and Complex 4 are greater than in other CTCs. The higher interaction energies decrease the intermolecular distances between the acceptor and these two donors in their CTCs, too. Finally, in the literature, CTCs can be ranked for their inherent charge transfer using the IP(donor) − |EA|(acceptor) offset value. A linear relationship between the magnitude of charge transfer and IP − |EA| was demonstrated (**Figure 4.11a**). We used the adiabatic ionization potentials of donor molecules (Table 4.4) and the adiabatic electron affinity of the acceptor molecule (**Table 4.4**) to obtain the IP − |EA| offset, as given in **Table 4.5**.

In situations where IP − |EA| offset is small, the CTCs are more ionic in character, allowing more charge transfer. Zhu et al. [84] showed that charge transfer vs. IP − |EA| plot falls onto a straight line for various CTCs containing 2,3,5,6 tetrafluoro-7,7,8,8-tetracyanoquinodimethane (F4-TCNQ). Similarly, when the NPA charge transfer for pairwise CTCs and IP − |EA| (**Table 4.4**) are plotted, a linear relationship is observed, as given in **Figure 4.11a**.

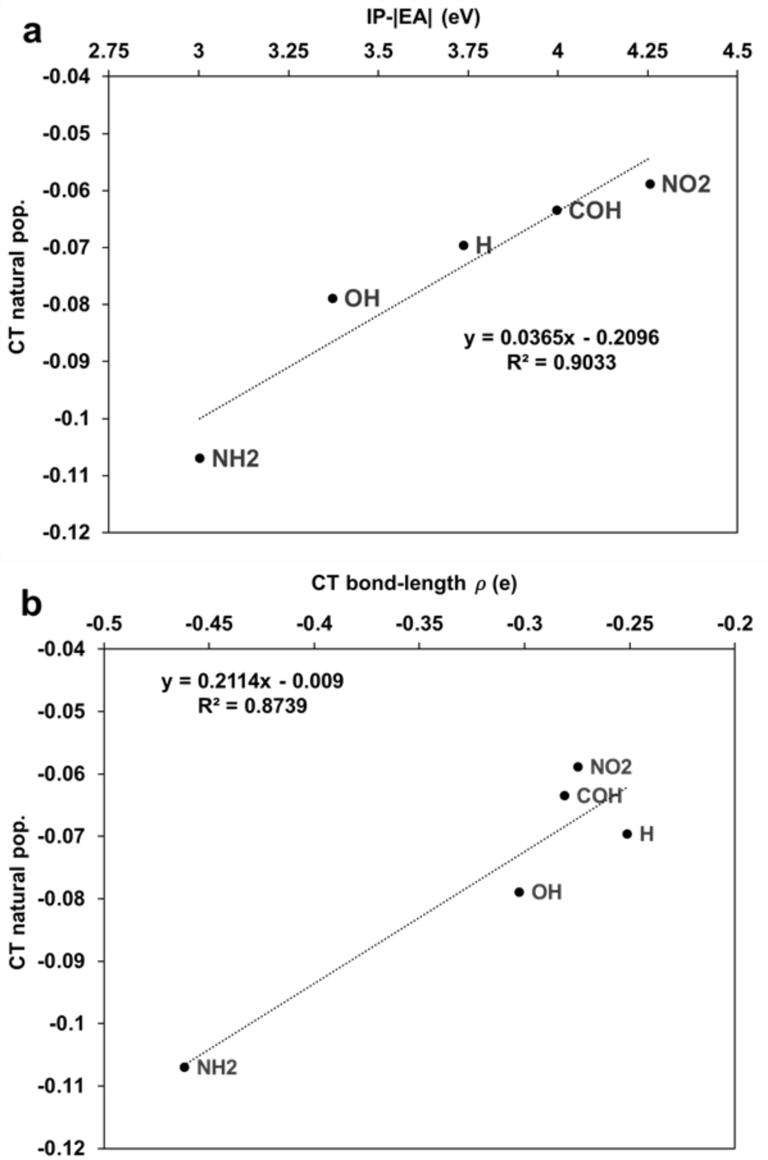

**Figure 4.11.** a) Correlation of IP−|EA| offset with the charge transfer based on NPA. b) Correlation of charge transfer from the bond lengths of acceptor (ρ) with the charge transfer based on the NPA.

**Table 4.6.** The bond lengths in the TCNQ acceptor obtained for the optimized geometry of neutral, anion and in pairwise interaction with donor at the M06-2X/6-311g(d) level.

| **Structure** | $\ell_1$ **(Å)** | $\ell_2$ **(Å)** | $\ell_3$ **(Å)** |
|---|---|---|---|
| Acceptor (anion) | 1.42877 | 1.41162 | 1.4241 |
| Acceptor (neutral) | 1.38492 | 1.42342 | 1.44636 |
| Acceptor- Donor(-$NH_2$) | 1.39664 | 1.42061 | 1.4363 |
| Acceptor- Donor(-OH) | 1.38792 | 1.42184 | 1.44323 |
| Acceptor- Donor(-H) | 1.38509 | 1.42278 | 1.44491 |
| Acceptor- Donor(-COH) | 1.38694 | 1.42245 | 1.44412 |
| Acceptor- Donor(-$NO_2$) | 1.38616 | 1.42191 | 1.4441 |

The bond length change in the TCNQ molecule can be utilized to predict the amount of charge transfer, too. To calculate the amount of charge transfer, ρ, from the bond length changes of TCNQ, we use the method proposed by Kistenmacher et al., explained in Section 3.3. **Table 4.6** shows that the interaction between TCNQ with donor molecules causes the lengthening of the double bond $\ell_1$ and the shortening of two single bonds, $\ell_2$ and $\ell_3$, as the most notable changes. When the charge transfer calculated by the bond length changes, CT bond length $\rho$ versus the charge transfer obtained by the NPA charges are plotted (see **Figure 4.11b**), a linear relationship emerges. In this relationship with the TCNQ acceptor, the amine-substituted pyrene, which shows the most improved charge dissipation performance in the charge decay experiments, surpasses the other pyrene derivatives.

With all the above CT value calculations and the displayed charge transfer trends, the relation was that the higher rates of charge decay on polymers were achieved with the CTCs with higher degrees of charge transfer.

### 4.4.3 The Effect of Photoexcitation in the Control of Contact Charging

Finally, we calculated the excited state properties of the binary complexes to elucidate the effect of photoexcitation of the CTCs via illumination. In the excited state, intermolecular distances decreased between the donor and acceptor molecules. This decrease is more pronounced for the hydroxy and amine substitutions (Fig. 4.12 a). Moreover, the most probable natural transition orbitals for the ground state to the first singlet excited state based on the highest oscillatory frequency and occupation were determined for both ground state and excited state geometries. Here, increased electronic transfer and coupling between molecules were observed via excitation by the structural change due to photoexcitation, as shown for amine substitution (**Figure 4.12b-c**). The main finding of the excited state calculations via illumination is on the HOMO-LUMO gap, for which the values calculated for the ground state binary complex geometry decreased dramatically for the hydroxy, followed by the amine substitutions in the excited state geometry due to the reduced intermolecular distances and electronic rearrangement in the excited state. One can expect enhanced dissipation of contact charges on polymers via illumination for the hydroxy and amine-substituted pyrene donor CTCs due to these decreased intermolecular distance, lowered band gap, and enhanced coupling with acceptor via photoexcitation.

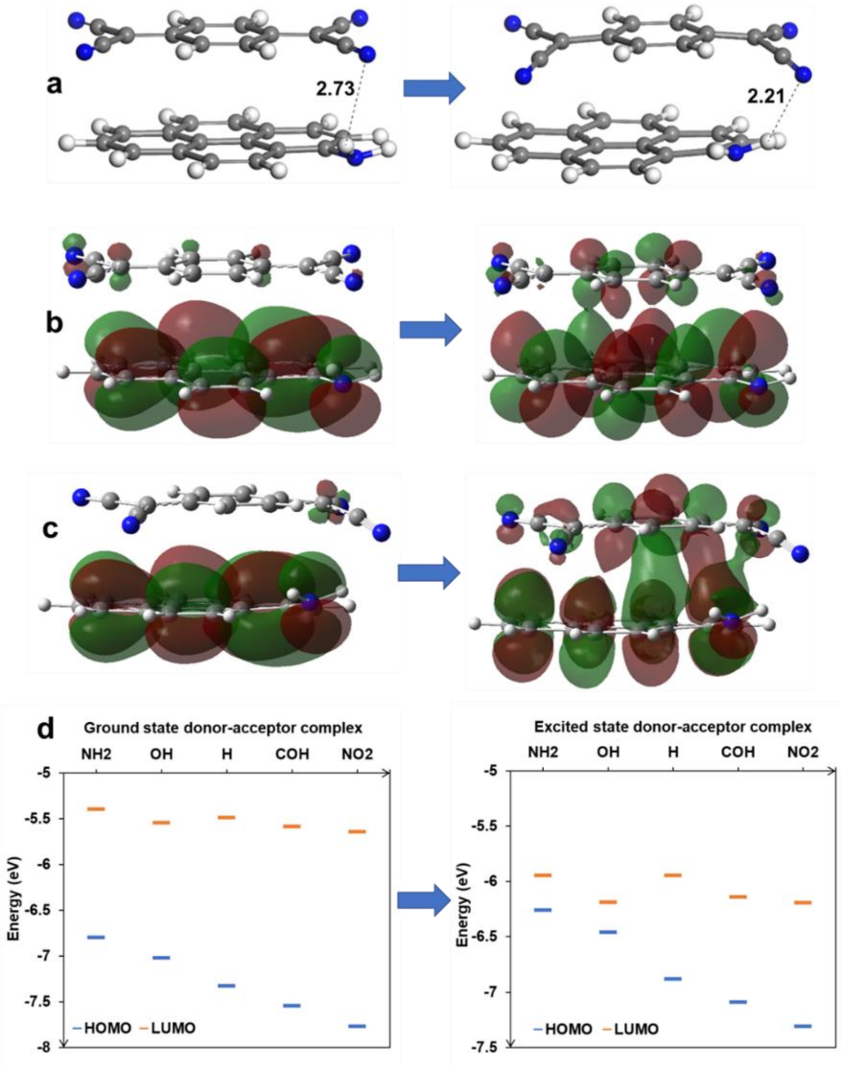

**Figure 4.12.** a) Optimized geometries for the ground state and first singlet excited state pairwise interactions for-$NH_2$ substitution, S0→S1 natural transition orbitals at the b) ground state optimized geometries and c) excited state optimized geometries, d) HOMO and LUMO energy levels for the ground state and excited state optimized geometries of binary complexes for different substitutions on the pyrene donor.

### 4.4.4 Exploring the Surface Potential of the CTC-doped Polymers with KPFM

As shown above, the dissipation of contact charges on a polymer (PDMS) is undoubtedly facilitated by the addition of the CTCs into the polymer. This is due to the charge transfer interactions in the CTCs, which can further be augmented by photoexcitation or using ‘better’ donors by changing the substitution on the pyrene. The discharge of the contact charges is linked in this way to the CT in the CTCs. However, what might be the exact mechanism that leads to charge dissipation? To get more insight into the mechanism of the discharging behavior of CTCs doped PDMS samples, we used KPFM surface potential mapping. We analyzed the surface of Complex 2 with this AFM modality, providing direct maps of the surface electrical potential values that can be used to track the location of charges and their relative magnitude spatially and temporally. The surface potential of the Complex 2-PDMS sample showed that PDMS and crystals could have either positive or negative potentials before contact with the Al foil (**Figure 4.13a**). Upon contact charging, the surface potential on the Complex 2 crystals increases to more positive values, and PDMS gains highly negative charges on it (**Figure 4.13c**). We first suspected that the fast charge decay on the Complex 2-doped PDMS sample was due to the interaction between opposite charges on the Complex 2 crystals and the PDMS polymer. To confirm whether opposite charging was the reason for fast decay, we decided to perform potential mapping on the Complex 1-PDMS surface. Like the uncharged Complex2-PDMS, Complex1-PDMS had either positive or negative potentials on the crystals and PDMS polymer **(Figure 4.13b**) before contact. After contact charging using Al foil, opposite charges developed on the crystals and polymer surface. Complex1 crystals gained highly positive charges, and PDMS surface gained highly negative charges (**Figure 4.13d**).

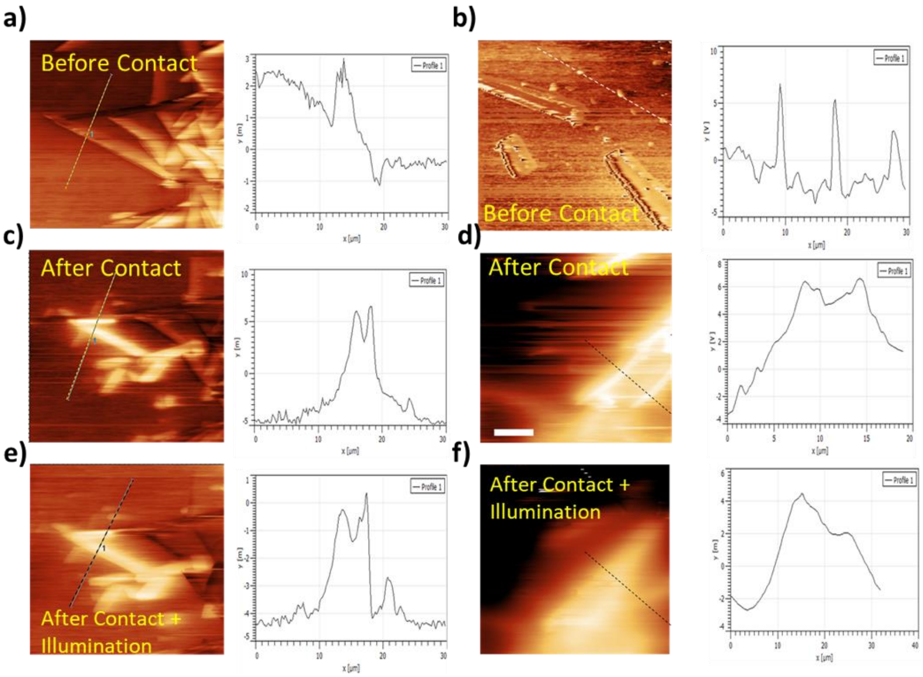

**Figure 4.13.** Kelvin Probe Force Microscopy surface potential maps of PDMS surfaces doped with Complex2 (left) and Complex1 (right) before contact, after contact charging, and charging followed by 2 min UV illumination. (The potential data are shown on the right for the dashed line crossing through the CTC domain in the corresponding images). The maps show, upon contact charging, CTC domain acquires positive and PDMS domains acquire negative potential. Upon illumination, the electric potential is reduced rapidly in both domains, in comparison to no decay in undoped PDMS in this time interval (not shown here). The decay rate is faster for Complex 2 doped PDMS, where the CTC domain charge drops to 0 V (from +5.0 V) upon illumination.

Then we retrieved KPFM surface potential maps of both surfaces after illuminating the surfaces with UV light. We observed positive potential on the sample with Complex 2; the electrical potential on the CTC crystals decayed rapidly to zero. However, on the crystals of Complex 1 in PDMS, such a significant potential decrease was not observed within the same time interval. Based on these observations, we can conclude that the co-existence of oppositely charged material domains at the nano level might imply that these domains neutralize each other. This neutralization is why we detect less charge at the macro level with the Faraday cup measurements. However, this is not the case because on the contact charged samples:1) at the macro level, samples are charged with a non-zero net charge, and more importantly, 2) both Complex 2-PDMS and Complex 1-PDMS surfaces exhibit oppositely charged (positively charged CTC and negatively charged PDMS) at the nanoscale. Still, there exists a substantial difference in their charge decay rates upon illumination. We envisaged that the fast charge decay of Complex 2-PDMS under UV illumination is due to the lowering of the HOMO-LUMO energy levels and the decrease in the band gap of Complex 2 in the excited state compared to the ground state. In other words, the charges on the Complex 2 dissipated due to fast electron transfer between a strong electron donor and a good electron acceptor (TCNQ). Decreasing the bandgap in the excited state of Complex 2 and increasing the degree of charge transfer render a fast-discharging pathway compared to its ground state in decay experiments. According to KFM mapping, the charges on Complex 1 were not diminished by UV irradiation as observed for Complex2. This result is probably due to the weaker electron donor ability of the unsubstituted pyrene (Complex 1) compared to the amino substituted pyrene derivative (Complex 2).

### 4.4.5 The Effect of Morphology of CTCs on their Ability to Act as a Charge Dissipator on Contact Charged Polymers

Since charge carrier mobility is affected significantly by the morphology of the self-assembled binary systems as demonstrated previously for PEDOT:PSS-based bulk heterojunction and thermoelectric materials [85], [86]. The packing motif and CTCs' morphological properties could have a substantial effect on the electrical conductivity and charge dissipation mechanism in this study, too. We performed SEM analyses of different cocrystals on the PDMS matrix. Complex 2 network can be expected to have a better network structure due to the strong hydrogen bonding (and thus a better charge carrier transport) compared to Complex 1, where this interaction is missing. In fact, the crystal structure of Complex1 indicates separate non-continuous single crystal domains on the PDMS surface (SEM, **Figure 4.14a**), while in Complex 2 nanofibrous continuous network forms on the polymer surface (SEM, **Figure 4.14b**). Therefore, one can expect that the above-mentioned enhanced charge dissipation for Complex 2 can also be affected by the pathways via interconnectivity of the grains.

In addition to the effect of CTC chemical bonding, the possible effect of the doping concentration on the morphology is shown in **Figure 4.6.** The morphology of low concentration (1.0 x $10^{-3}$ M) of Complex 2 on PDMS in **Figure 4.14c** lacks micron-sized stacks of self-assembly in the system that exist in the samples with higher doping concentration (1.0 x $10^{-2}$ M). This can explain the decreased contact charging efficiency in the low concentration sample compared to the concentrated sample with the higher charge dissipation.

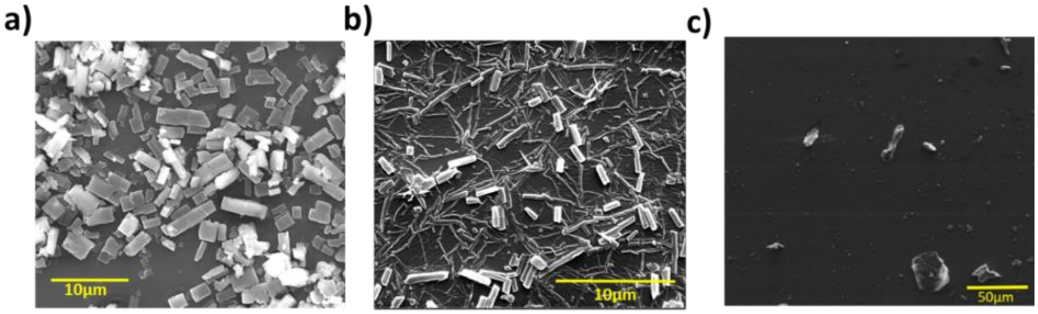

**Figure 4.14.** CTC morphology. The SEM images of (a) Complex 1 and (b) Complex 2 doped PDMS, doped from 1.0 x $10^{-2}$ M CT assembly solutions in dichloromethane. Interconnectivity through needle-like CTC morphology in (b) may contribute to faster charge dissipation mediated by this CTC. c) Complex 2-doped PDMS, doped from 1.0 x $10^{-3}$ M CT assembly solutions in dichloromethane does not display any micron-scale stacks of the CTC.

While Complex 2 fits in the second-order kinetic at high humidity (RH = 40-55%, **Figure 4.4**), Complex 2 obeys the first-order kinetic at low humidity (RH = 15-30%, **Figure 4.5**). Such a dissipation mechanism might involve other competing pathways to discharge the contact charging, including the formation of hydrogen bonding between the CTCs and water vapor on the surface.

## 4.5. Conclusion (Part A)

We report;

1) The faster dissipation of contact charges on a polymer (PDMS) doped with CTCs than on the undoped PDMS.

2) The fast dissipation observed in the presence of CTCs can further be facilitated by photoexcitation of the samples or using 'better' donors by changing the substitution on the pyrene.

3) The fast dissipation observed in the presence of CTCs is not because of an overall surface conductivity increase; the surfaces remain insulators after doping and under illumination.

4) The morphology, concentration**,** and humidity can contribute to efficient charge dissipation.

5) As supported by KPFM maps, the charge dissipation is **physically mediated through the structure's CTCs**.

With all these findings, we propose a novel charge dissipation method using CTCs in common polymers as additives. The method uses minute amounts of CTCs that can be doped into the polymers, immersing the polymers into the CTC solutions. The new charge dissipation method can be chemically tuned, remotely controlled by light, and does not change the overall electrical conductivity of the material.

# PART B

## Chapter 5

## 5. Introduction to Colloidal Semiconductor Nanocrystals

QDs are a class of semiconductor nanomaterials. A QD particle has hundreds to thousands of atoms, making the diameter of the particle range from 2 to 20 nanometers [87]. QDs exhibit a quantum confinement effect and has wide tunability of their band gaps [88], [89], [90]. The generation of electron-hole pairs in these nanocrystals makes them desirable materials in optical and electronics applications, including photovoltaic devices [91], biosensing [92], and photocatalysis [93], as well as in other energy applications, such as triboelectric nanogenerators [94], [95]. In this chapter, we introduce quantum confinement and the surface effect. We describe the synthesis of QDs, their classifications, and our aim of using QDs in the dissipation of contact charges on polymer surfaces.

### 5.1 Quantum Confinement

In bulk semiconductors, there are continuous energy states of valance and conduction bands, and there is a corresponding energy gap between these bands, known as the band gap. Energy is required to excite an electron to the conduction band from the valence band. When the excitation energy is higher than the band gap, the electron is excited to the conduction band, leaving a hole in the valence band. The energy state at which the electron-hole pair has the minimum energy is called an exciton. The distance between the electron-hole pair is called the Bohr radius. In an electric field, the charge carriers can become mobile and create a current. With the radiative recombination of the electron and hole, the energy is emitted as a photon. If the radius of the semiconductor nanocrystal is smaller or equal to the Bohr radius, the mobility of the electron and hole are spatially confined through the dimension of nanocrystals. The energy difference between the two levels exceeds the $K_BT$ ($K_B$ is Boltzmann constant, T is temperature), and the mobility of electron and hole is restricted to the nanocrystal dimensions. This case describes the confinement of the electron and hole pair in the Bohr radius in the nanocrystal, known as quantum confinement.

[96]. Therefore, QDs have discrete energy levels and size-dependent absorption and emission wavelengths depending on their size and shape (**Figure 5.1**).

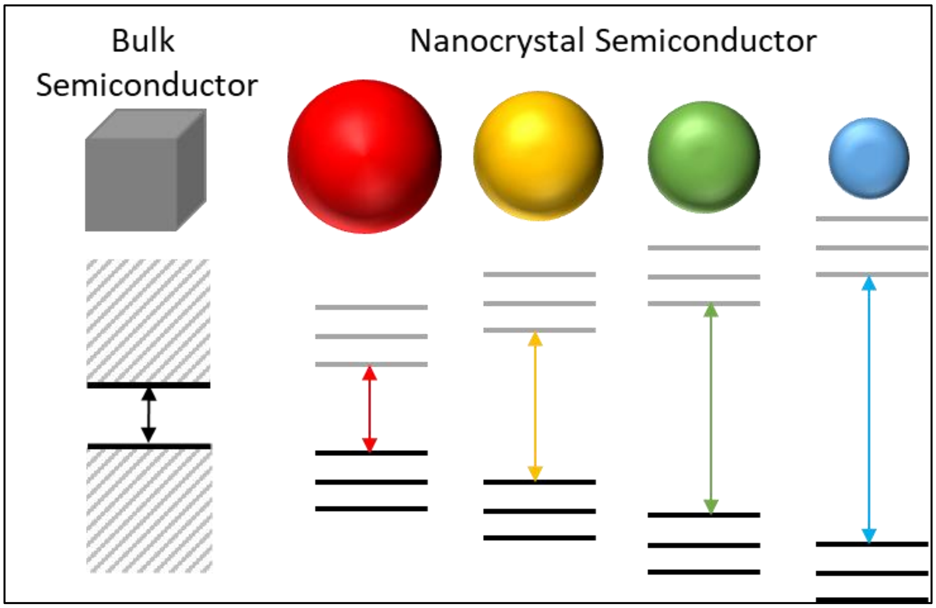

**Figure 5.1.** The schematic illustration of the energy variation for bulk and nanocrystal semiconductors. In the nanocrystals, the absorption wavelength depends on the crystal size with an inverse relation.

## 5.2 The Surface Effect

Quantum dots (QDs) have a large surface-to-volume ratio owing to their small size. Surface atoms do not have full coordination numbers. The surface has non-radiative channels and traps states to trap the radiative carriers. QDs can get easily oxidized if their surfaces are not passivated. Thus, colloidal quantum dots are covered with organic molecules (ligands) to passivate their surface (**Figure 5.2**). In some cases, the steric repulsions of the ligand molecules at the surface of the quantum dots can cause under-coordination of the surface atoms of QDs, leading to poor coverage of the atoms. For that reason, these QDs are passivated by growing another, more chemically stable inorganic semiconductor material on their surfaces [11 97]. This type of structure is known as core/shell QDs. The shell passivation of the QDs inhibits the undesired surface charge recombination processes, e.g., electron-hole recombination at the surface defects and Auger recombination processes. The passivating shells enhance the stability of the bare inorganic nanocrystals and increase their energy harvesting efficiency. In addition, the fluorescent quantum yield and photostability of QDs are improved by the shells. [97], [98], [99]. To successfully synthesize and achieve shell passivation, the crystal lattice mismatch must be avoided. The type of shell material which can generate defect states due to any lattice strain through the core/shell interface should be avoided.

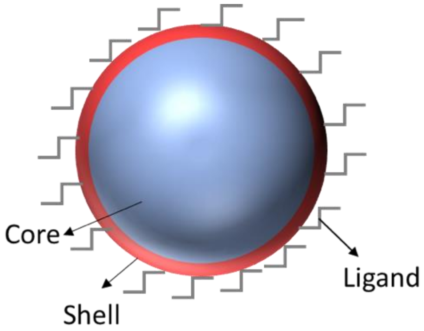

**Figure 5.2.** The schematic illustration of a colloidal quantum dot with a passivating inorganic shell and organic ligands.

## 5.3 Synthesis of Semiconductor Nanocrystals

Synthesis of the core/shell QDs includes two primary step processes: synthesis of the core QDs and the subsequent shell growth process. Solvents, precursors, and organic surfactants are used to synthesize colloidal QDs. In the first step, nucleation, the precursor is chemically converted to the monomers (active atomic and molecular species) by increasing the temperature in an inert atmosphere. The growth of monomers into the size-defined nanocrystals is controlled by adding surfactant molecules at a given time during the growth step.

Specialized techniques are used to obtain precise size control. The hot injection technique was introduced by Murray et al. in 1993 to allow narrow size dispersity and the rapid creation of a product from a combination of metal and chalcogen precursors [100]. The stable colloidal is formed when the appropriate concentrations of precursor and ligand are used. Colloidal particle formation is initiated by supersaturation, which leads to homogeneous nucleation. The homogeneity of the nucleation was explained theoretically in the 1950s [101]. To obtain size monodispersity, each particle must be at the same temperature for growth, which is possible at higher temperatures. Singular nucleation events are achieved by a massive surge in supersaturation by rapid injection of the precursor in a hot bath of solvent and ligand. Although the method can deliver the desired monodispersity of particle sizes, the hot-injection method could not be applied in all material families, such as III-V and Group IV materials.

An alternative method is the non-injection method. It was introduced by Pradhan et al. to synthesize QDs at low temperatures using a single compound precursor (metal xanthate) [102]. Different sizes of QDs can be obtained by adjusting the temperature or concentration. The single-source inorganic cluster approach is another non-injection method that uses the single-source precursor [103].

Once the core is formed through one of the above methods, the shell can be formed on the core. The shell's thickness is critical to protecting the surface of QDs. The passivation may not be fully achieved if the shell is too thin. If the shell is too thick, it may create defect states due to a lattice strain. Therefore the shell thickness has to be controlled, and this can be done by controlling the number of deposited monolayers.

'm' monolayers of shell thickness for the volume of the shell material is calculated as:

$$\mathbf{V}_{\boldsymbol{Shell}} = \frac{\mathbf{4}}{\mathbf{3}}\boldsymbol{\Pi}[(\boldsymbol{r_C} + \boldsymbol{m}\ \boldsymbol{x}\ \boldsymbol{d_{ML}})^{\mathbf{3}} - \boldsymbol{r_C}^{\mathbf{3}}]$$

$V_{Shell}$= Volume of the shell material

$r_C$= the radius of the core QDs

$d_{ML}$= the shell thickness for one monolayer (ML, nm)

the amount of shell material, $n_{shell}$ in moles required to deposit 'm' mL shell:

$$\mathbf{n}_{\boldsymbol{Shell}} = \frac{\mathbf{V}_{\boldsymbol{Shell}}\ \mathbf{x}\ \mathbf{D}_{\boldsymbol{core}}\mathbf{x}\ \boldsymbol{N_A}\ \boldsymbol{x}\ \boldsymbol{n_{QD}}}{\boldsymbol{MW_{core}}}$$

$D_{Core}$= the density of the core material

$N_A$= the Avogadro's number

$n_{QD}$= the number of moles of the core QDs in solution

$MW_{core}$= molecular weight of the core material

For the growth of the shell, the Successive Ionic Layer Adsorption and Reaction (SILAR) method allows the deposition of the precise amount of the material to achieve the desired shell thickness, which can be calculated using the above equations. One monolayer of the shell can be deposited at a time upon injecting the precursors (cationic and anionic) into the core solution. Monodisperse and highly luminescent core/shell QDs could be synthesized by this method [104].

## 5.4 Classification of the Core-Shell Semiconductor Nanocrystals

The semiconductor nanocrystals can be classified according to the nature of the band gap and the electron transfer pathways they possess, which can be tuned with ‘bandgap engineering’. Alteration of the band alignments allows the control of the electron transfer pathways by changing spatial delocalization in the semiconductors [105]. Typical classes of QDs are named type-I and type-II (**Figure 5.3**). The former has the electron and hole localized in the core semiconductor. This localization enhances the fluorescence quantum yield by reducing any interaction between the surface states with the exciton. When the narrower bandgap is on the shell material, it is called ‘inverted type-I’, which cannot provide the same isolation. Type-II QDs have localized holes on the one material with a higher-lying valence band, while the electrons are localized on the other material with a lower-lying conduction band. The relative alignment of the conductive and valance band edges decreases the wave function overlap of carriers, hence decreasing the QY. The quasi type-II has delocalized holes or electrons in both semiconductor heterostructures, whereas the other carrier (electron or hole) is localized only in the other material. In that case, the conduction or valance bands in core and shell materials have the same energy [106].

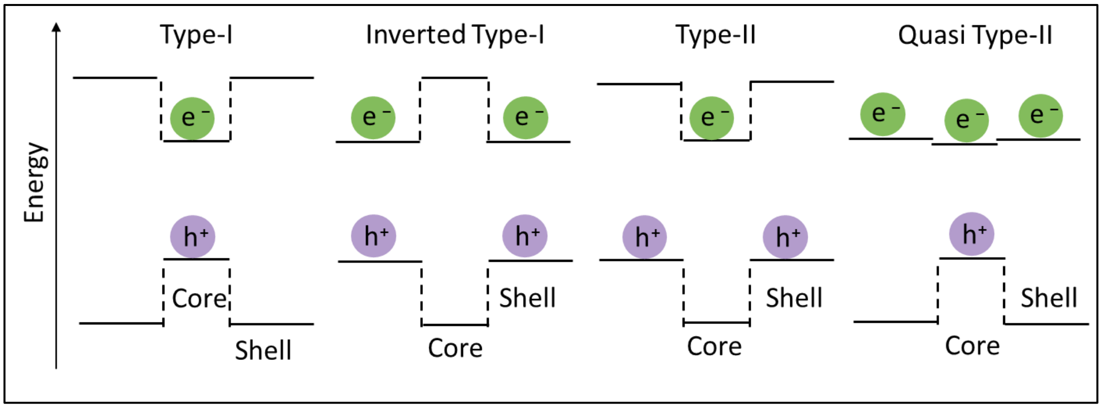

**Figure 5.3.** The schematic illustration of the relative positions of conduction and valence band energies in different core/shell QD heterostructures.

## 5.5 The aim of using QDs as Additives for Dissipation of Contact Charges on Polymers

In this part of our study, the role of QDs in triboelectric charge mitigation on polymers will be displayed. Previously, in a study from our group, a remote dissipation of contact charges on common polymers was achieved [51]. In that study, organic dyes were used to dissipate charges on the polymers as mediators in the dissipation mechanism. It was shown that the photoexcitation of the dyes resulted in an increase in the dyes' dipole moments, which helped to dissipate the charges. The dyes were effective quenchers of contact charges; however, owing to the poor photostability, they cannot be used as long-term antistatic agents. Therefore, QDs stand as better antistatic dopant alternatives in terms of their high photostability. Also, a better understanding of the charge dissipation mechanism can be obtained if a series of quantum dots are used with different band gaps and electronic transitions: Here, the versatility is quite rich: different atoms, sizes, types (core or core/shell), and geometry QDs can be involved in exploring the mechanism. The interactions between the polymer matrices and the QDs can be tuned with the different capping ligands of different lengths or chemistries. This cornucopia of possibilities is impossible to explore in one thesis work. Therefore, we chose to study two possible sets, changing the size and the type of the QDs, and monitoring the effect of different types of core/shell structures in the dissipation of contact charges.

In this study, the polymer discharging effect in the two different systems (solvent and solid) was investigated for CdSe with varying sizes. Then, the effect of various localizations of charge carriers (hole and electron) on polymer discharging was investigated using different core/shell QD heterostructures, type-I, and quasi-type-II. The interaction of mechanospecies on contact charged polymers with these carriers was investigated to enlighten the charge dissipation mechanism.

# Chapter 6

## 6. Control of Contact Charging of Polymers with Quantum Dots

In this part of our study, the effect of QDs, with different sizes and types of heterostructures in polymer contact charging was investigated in the solid and solvent systems. Electron-hole pairs could quickly be generated in Cd-based QDs prepared from the II-VI group of semiconductors [107]. Therefore, first, a common core nanocrystal, CdSe, was studied. Then, to obtain core-shell nanocrystal, a common shell material having wide bandgap, ZnSe, was decorated as the shell on the previously studied CdSe dots [108], forming CdSe/ZnSe core-shell QDs. Below, the synthesis of the core and core/shell QDs, the preparation of QD-doped PDMS, the characterization of QDs, and the results of charging/discharging experiments in the dark and under UV illumination are described. Finally, we present a mechanism to explain our observations on the control of contact charging of polymers with the QDs. The proposed mechanism involves electron transfer between the mechanospecies (mechanoanions, mechanocations, and mechanoradicals) on charged polymers and the QDs.

### 6.1 Experimental

The different sizes of core CdSe (2.5 nm and 3.5 nm), and core/shell QDs - CdSe (2.5 nm)/ZnSe (3 monolayers (ML)) and CdSe (3.5 nm)/ZnSe (3 monolayers (ML)) with different heterostructure (type-I and quasi-type-II) were used and characterized throughout this thesis. Then, QDs were doped into the common polymer, PDMS, to investigate the charge dissipation effect of the QDs in the solid polymer. In another set of experiments, the solutions of QDs were dropped in the vials with contact-charged PTFE beads in hexane, probing the charge dissipation effect of the QDs in the solution.

### 6.1.1. Preparation and Characterization of the Quantum Dots

Core CdSe QDs varying sizes (2.5 nm, and 3.5 nm) and core/shell (type-I and quasi type-II) were synthesized by Firdevs Aydın at Middle East Technical University, Chemistry Department. CdSe core QD of 3.5 nm ($\lambda_{abs,max}$ = 568 nm) was used for

CdSe/ZnSe type-I QDs, and CdSe core QD of 2.5 nm ($\lambda_{abs,max}$ = 518 nm) was used for CdSe/ZnSe quasi-type-II QDs as the core materials according to a theoretical study [109].

A qualitative picture of the relative energies of the conductive and valence bands of these core-shell QDs is given in **Figure 6.1a**. The UV-Vis and the photoluminescence spectra of these QDs in hexane are shown in Fig. 6.1b and c. The absorption and photoluminescence (PL) wavelength maxima and the quantum yield values of the prepared QDs are given in **Table 6.1.**

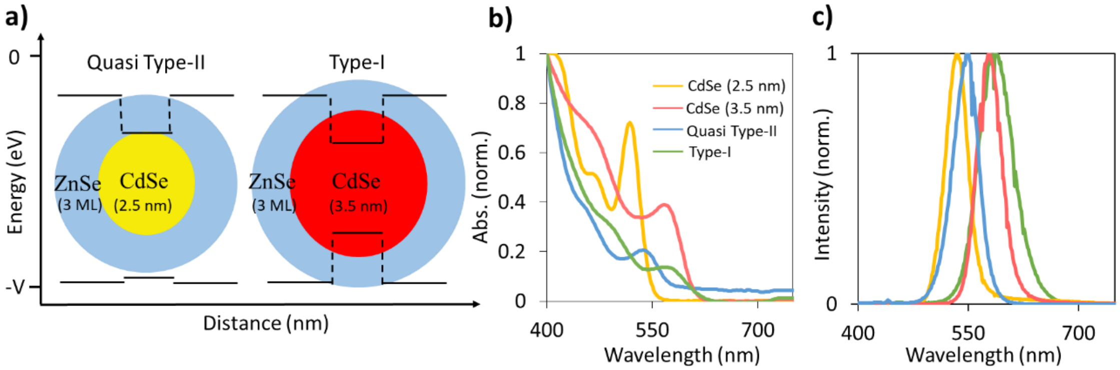

**Figure 6.1**. a) The schematic diagram of CdSe/ZnSe core/shell QDs with different band gaps. b) The UV-Vis spectra and c) The PL spectra of QDs in hexane; CdSe 2.5 nm (yellow), CdSe 3.5 nm (orange), CdSe/ZnSe Type-I (green), and CdSe/ZnS Quasi-Type-II (blue) ($\lambda_{exc}$= 390 nm). The prepared quantum dots solutions were used fresh and stored in a nitrogen filled glove box.

**Table 6.1.** The maximum absorption and emission wavelength of the QD solutions

| **QD** | **Size** | **Absorption λ max** | **Emission λ max** | **Quantum Yield*** |
|---|---|---|---|---|
| CdSe | 2.5 nm | 518 nm | 536 nm | 3.80 % |
| CdSe | 3.5 nm | 568 nm | 579 nm | 1.21 % |
| CdSe/ZnSe (Quasi Type II) | Core 2.5 nm, shell 3ML | 536 nm | 550 nm | 27.4 % |
| CdSe/ZnSe (Type I) | Core 3.5 nm, shell 3ML | 574 nm | 587 nm | 58.5 % |

* = Measured and calculated by Firdevs Aydin at METU.

The PL decay characteristics of core and core/shell QDs are shown in **Figure 6.2a**, and the lifetime data retrieved from the decay plot of QDs are shown in **Table 6.1**. For the calculation of the lifetime data, the decays were fit with a triple-exponential function. The presence of a third component ($t_3$) in the decays of the core CdSe QDs (2.5 nm and 3.5 nm) indicates the existence of some deep trap states in these QDs [110]. The third component was not observed when these trap states were passivated with the formed shell (core/shell nanocrystals). The intensity average PL lifetime was calculated according to below equation:

$$\boldsymbol{\tau_{ave}} = \frac{\boldsymbol{A_1\tau_1{}^2 + A_2\tau_2{}^2 + A_3\tau_3{}^2}}{\boldsymbol{A_1\tau_1 + A_2\tau_2 + A_3\tau_3}}$$

The XRD spectra are shown in **Figure 6.2b**. For XRD analysis, quantum dots in hexane were drop-cast onto a silicon wafer (black). The samples were irradiated by copper Kα with 1.5418 Å wavelength. There is a shift to higher angles when the CdSe is passivated by the ZnSe shell, indicating the shell growth and the lattice compression of the core [111], [112]. The XRD peaks of CdSe 25.55, 42.57 and 49.66 refer to the lattice planes of (110), (220), and (311) of zinc blende CdSe (JCPDS No. No. 00-019-0191). The XRD peaks of the CdSe core shifted to larger angles after the growth of the ZnSe shells (JCPDS No. 00-037-1463). TEM images show the morphology of QDs including their size, shape and assembly. The

QDs solutions were diluted to prepare TEM images. 1-2 drop of QDs were dropped onto the copper mesh grids. The corresponding EDX proves the addition of the ZnSe shell on the CdSe core in the core/shell nanoparticles (**Figure 6.3**).

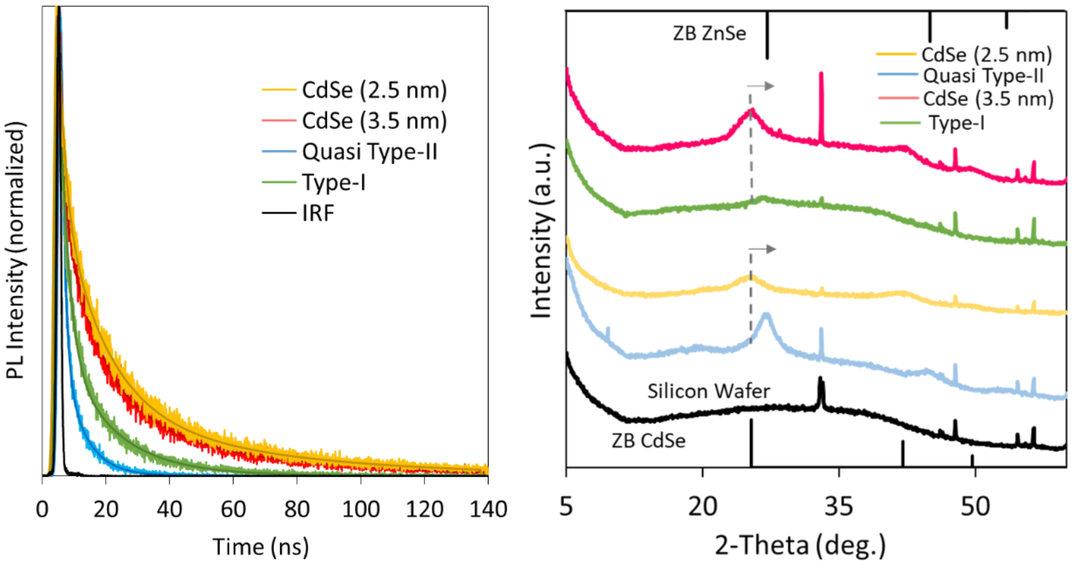

**Figure 6.2.** a) Time-resolved Fluoresence Intensity plot of the prepared QDs in hexane at room temperature. CdSe 2.5nm (yellow), CdSe 3.5nm (red), CdSe/ZnSe Type-I (green), CdSe/ZnSe Quasi-Type-II (blue), and prompt (black). b) The X-ray diffractogram of CdSe 2.5 nm (yellow) and 3.5 nm (red), and CdSe/ZnSe Quasi-Type-II (blue), and Type-I (green) (zinc blende CdSe (JCPDS No. No. 00-019-0191), ZnSe shells (JCPDS No. 00-037-1463)).

**Table 6.2**. Lifetime components of the CdSe QDs (2.5 nm and 3.5 nm) and of the corresponding shelled QDs, CdSe/ZnSe (3 ML) (quasi type-II, type-I).

| QDs | $A_1$ | $\tau_1$ (ns) | $A_2$ | $\tau_2$ (ns) | $A_3$ | $\tau_3$ (ns) | $\tau_{ave}$ (ns) | $\chi^2$ |
|---|---|---|---|---|---|---|---|---|
| CdSe (3.5 nm) | 38.23 | 11.30 | 7.08 | 1.18 | 54.69 | 44.73 | 39.60 | 1.04 |
| CdSe (2.5 nm) | 41.30 | 13.68 | 8.00 | 2.02 | 50.70 | 54.22 | 47.09 | 1.03 |
| CdSe/Znse (Type-I) | 34.33 | 2.60 | 65.67 | 15.78 |  |  | 14.73 | 1.20 |
| CdSe/Znse (Quasi-type-II) | 46.11 | 1.01 | 53.89 | 6.63 |  |  | 5.98 | 1.01 |

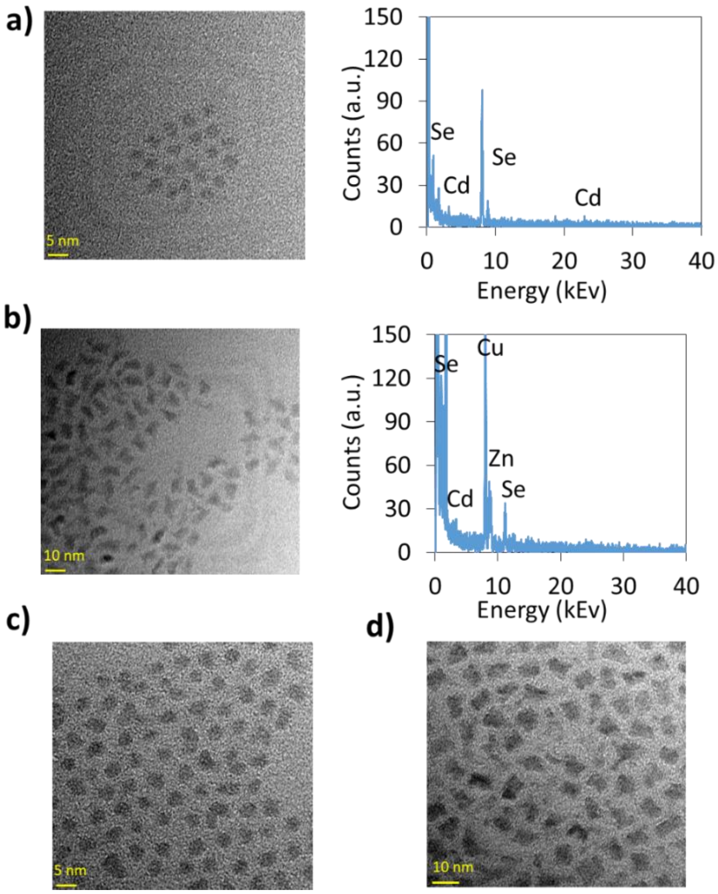

**Figure 6.3**. TEM images and the corresponding EDX spectra of a) CdSe 2.5 nm, b) CdSe/ZnSe quasi type-II, c) CdSe 3.5 nm d) CdSe/ZnSe (Type-I)

### 6.1.2 Preparation and Characterization of the QD-doped PDMS

Base polymer and curing agent of PDMS (Sylgard 184) were mixed in a 10:1 ratio. This prepolymer mixture was kept for two hours under low pressure. Then, 1 mL solution (5 mg/mL in hexane) of the QDs was added to the two-hour-aged prepolymer with vigorous stirring to obtain homogenous samples. The nanocomposite mixture was transferred to polystyrene petri dishes. The petri dishes were kept under vacuum to remove $H_2$ (g) formed during the polymerization reaction and the bubbles created during the mixing. Curing was completed in 24 hours at 70°C. 1.40 mm thick, round (1.7 cm diameter), and flat samples were cut from the cured polymer as samples for the tapping experiments (**Figure 6.4**).

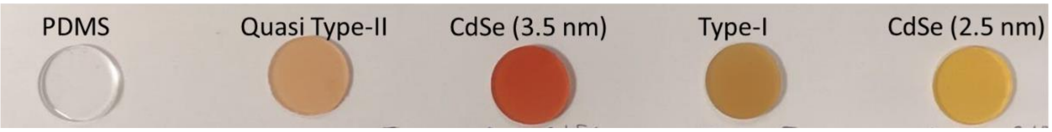

**Figure 6.4.** QD doped PDMS samples

The UV-Vis spectra of QD-doped PDMS samples are shown in **Figure 6.5**. When the core was passivated by the shell, the red shift was observed for the absorption maxima. To investigate the morphology of QD-composites SEM imaging technique was utilized (**Figure 6.6)** with an accelerating voltage of 30 kV.

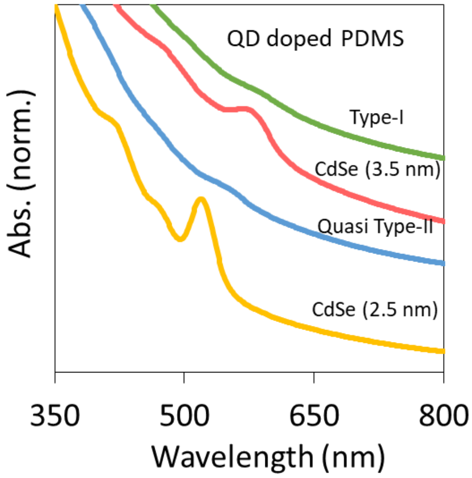

**Figure 6.5.** UV-Vis spectra of the QD-doped PDMS samples.

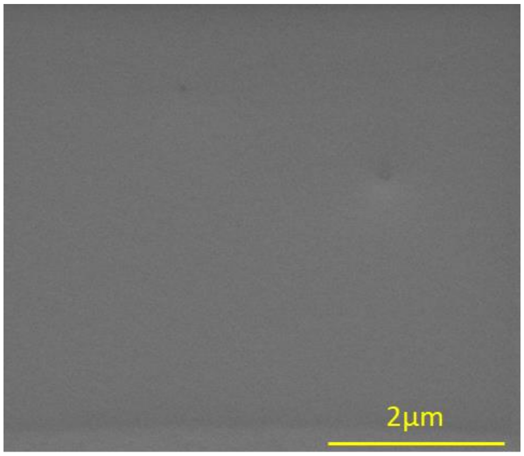

**Figure 6.6.** An example of a SEM micrograph of the QD doped PDMS samples showing the flat surface of the sample.

We measured the surface conductivities of our QD-doped PDMS samples which is described in Section 2.4 Instrumental Techniques. The values fit in the insulator range, 1.34 x $10^{-16}$ S, 1.85 x $10^{-16}$ S, 2.35 x $10^{-16}$ S, and 1.43 x $10^{-16}$ S for CdSe (3.5 nm), CdSe (2.5 nm), Type-I, and Quasi Type-II doped PDMS, respectively. These values did not change significantly under UV illumination - 1.28 x $10^{-16}$ S, 2.06 x $10^{-16}$ S, 2.26 x $10^{-16}$ S and 1.57 x $10^{-16}$ S for CdSe (3.5 nm), CdSe (2.5 nm), Type-I and Quasi Type-II doped PDMS, respectively (**Table 6.3**).

**Table 6.3**. The surface conductivity values of the nanocrystal-doped and the undoped PDMS samples. For the conductivity measurement, three identical samples were prepared and the conductivity values are calculated by averaging of these three samples.

| Material | Conductivity (S) | |
|---|---|---|
| | Dark | UV |
| (3.5 nm) CdSe<br>5 mg | $1.34 \times 10^{-16}$ | $1.28 \times 10^{-16}$ |
| (2.5 nm) CdSe<br>5 mg | $1.85 \times 10^{-16}$ | $2.06 \times 10^{-16}$ |
| Type-I<br>5 mg | $2.35 \times 10^{-16}$ | $2.26 \times 10^{-16}$ |
| Quasi Type-II<br>5 mg | $1.43 \times 10^{-16}$ | $1.57 \times 10^{-16}$ |
| (3.5 nm) CdSe<br>10 mg | $1.49 \times 10^{-16}$ | $1.79 \times 10^{-16}$ |
| Type-I<br>10 mg | $1.91 \times 10^{-16}$ | $1.70 \times 10^{-16}$ |
| PDMS | $1.33 \times 10^{-16}$ | $1.09 \times 10^{-16}$ |

## 6.2 Charge Decay

### 6.2.1 Charge Decay Experiments of the QD-doped PDMS

The decay setup was described in **Figure 2.2b** and Section 2.3.1 Charge Decay Measurements of Solid PDMS. First, the core nanocrystal having different band gap energies were used as dopants in PDMS. When the pieces were doped with 3.5 nm-sized CdSe nanocrystals (5 mg/6 g polymer), the decay profile did not change significantly in dark. Illumination with UV light did not affect the decay, either. In numbers, the decay rate of 3.5 nm size CdSe nanocrystals doped PDMS (0.04± 0.01 $s^{-1}$) was close to that of undoped PDMS in dark and UV (0.05± 0.02 $s^{-1}$ and 0.06± 0.01 $s^{-1}$ **Figure 6.7a**). The 2.5 nm CdSe nanocrystals doped into the PDMS sample showed a slightly faster decay (0.09± 0.02 $s^{-1}$) rate than undoped PDMS (0.06± 0.01 $s^{-1}$), by illumination with UV light (**Figure 6.7a**, yellow dashed line).

On the other hand, a different picture comes into play with the core/shell QDs. The decay rate of type-I doped PDMS samples (0.24± 0.02 $s^{-1}$) increased by four in the dark compared to the undoped control samples. More surprisingly, the decay rate dramatically decreases in the presence of UV light (0.11 ± 0.11 $s^{-1}$). Finally, with the quasi-type-II doped PDMS, the contact charge decay rate significantly increased (0.23 ± 0.04 $s^{-1}$) in the dark and increased to 0.30 ± 0.06 $s^{-1}$ under UV illumination. The different amounts of QDs (1 mg and 10 mg) were doped into PDMS, indicating the same trend in dark and UV (**Figure 6.7c-d**), yet 10 mg doped PDMS samples were found to be similar to 5 mg doped PDMS samples. The decay rates are shown in **Table 6.3**.

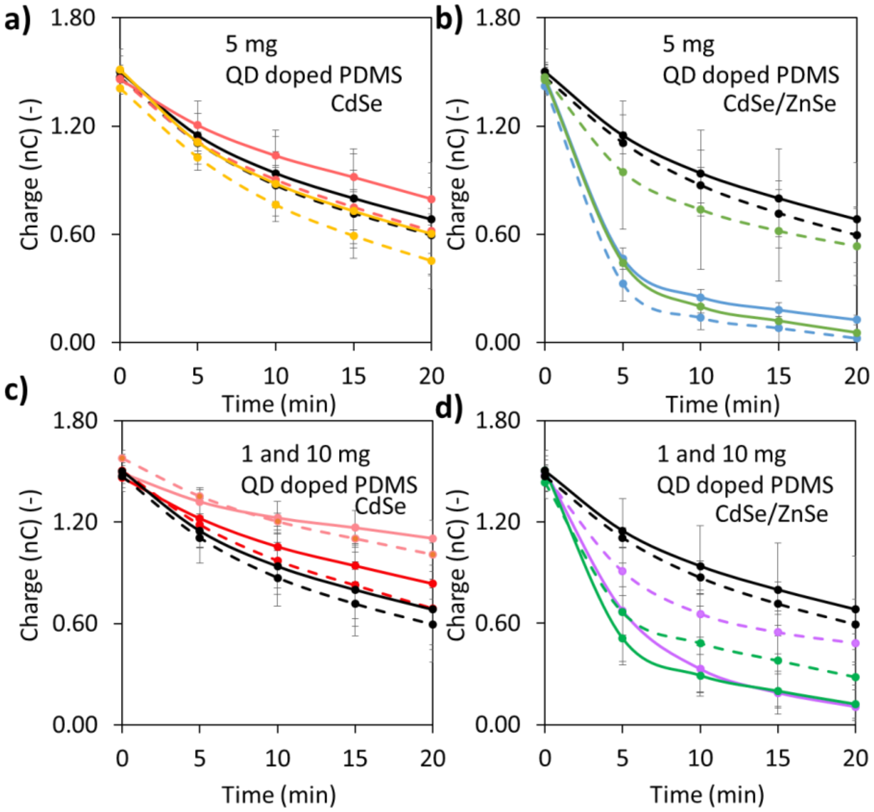

**Figure 6.7.** Contact charge decay on PDMS doped with the core CdSe and core/shell CdSe/ZnSe QDs in air. a) 3.5 nm (red), 2.5 nm (yellow) size CdSe doped and Undoped PDMS (black) in dark (solid line) and under illumination with UV (dashed line). b) Type-I doped PDMS samples (green), and Quasi Type-II doped PDMS samples (blue) under dark and UV illumination. c) The charge decay on different doping amounts of 3.5 nm sized core QDs, 1.0 mg (red) and 10 mg (pink)) in dark and UV d) The charge decay on different doping amounts of Type I CdSe/ZnSe QDs, 1.0 mg (purple) and 10 mg (green)) Error bars correspond to standard deviations determined from three independent experiments for each condition. The discharge experiments were obtained in 18-22% RH.

**Table 6.3.** The decay rate of QD doped and undoped samples calculated by a first order fit on the first five minutes data in the decay plots in **Figure 6.7**.

| First Order Kinetic (0-5 min) | Decay Rate ($s^{-1}$) | | |
|---|---|---|---|
| Sample | 1mg | 5mg | 10mg |
| (3.5 nm) CdSe Dark | 0.02±0.00 | 0.04±0.01 | 0.04±0.00 |
| (3.5 nm) CdSe UV | 0.03±0.00 | 0.05±0.02 | 0.03±0.01 |
| Type-I Dark | 0.16±0.08 | 0.24±0.02 | 0.22±0.07 |
| Type-I UV | 0.09±0.04 | 0.11±0.11 | 0.16±0.08 |
| (2.5 nm) CdSe Dark | | 0.06±0.01 | |
| (2.5 nm) CdSe UV | | 0.09±0.02 | |
| Quasi-Type-II Dark | | 0.23±0.02 | |
| Quasi-Type-II UV | | 0.30±0.06 | |
| PDMS Dark | 0.05±0.02 | | |
| PDMS UV | 0.06±0.01 | | |

### 6.2.2. Charge Decay Experiments with Polymers in contact with CTC Solution

Finally, we studied the discharging effect of the QDs in hexane. Since the polymer doping experiments provided interesting trends for the core/shell QDs, we performed the solution experiments with these QDs, particularly. As described in Section 2.3.2 Charge Decay Measurements of Polymer Beads in a Solvent, we first introduced 35 beads in each glass vial with 7 mL anhydrous hexane. Then the beads were mechanically contact-charged using a vortexer for 30 seconds. This rotational agitation caused the beads to stick onto the inner wall of the glass vial by electrostatic attraction. Using this method, contact-charged beads retain their charges for many hours. After vortexer charging, 10µl QD solution (0.2 mg/ml, anhydrous hexane) of different types of nanocrystals is dropped into the hexane. Control discharging experiments were done under the same conditions (RH = 15-25%), injecting the same amount of anhydrous hexane using the same volume and the same number of PTFE beads. PTFE beads were discharged in the first few minutes after adding

CdSe/ZnSe (quasi type-II) QD solutions into the vial (**Figure 6.8**). In the samples where only anhydrous hexane was injected, there was no discharge for days.

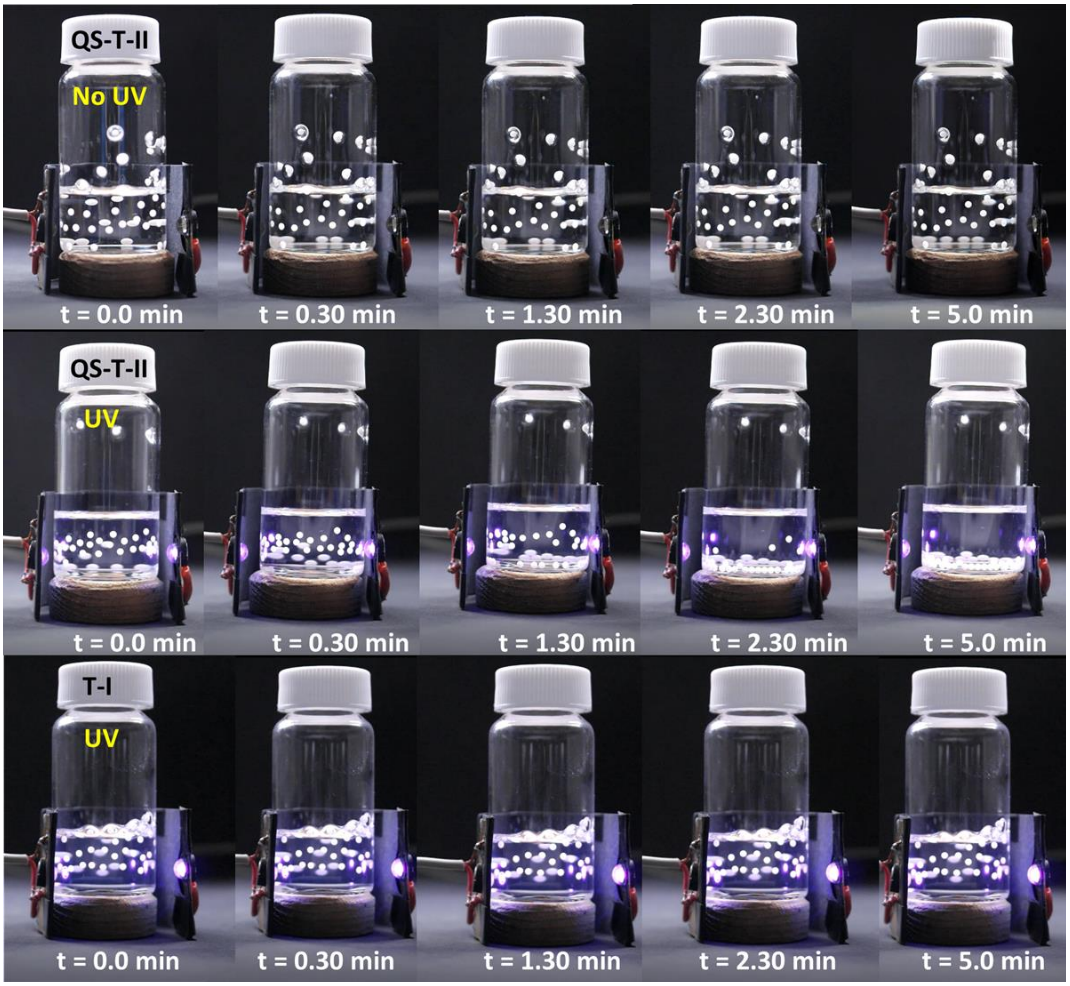

**Figure 6.8.** a) The number of discharged beads at the marked times after the QD solutions, quasi type-II (QS-T-II), and type-I (T-I), were added into the hexane in dark and with UV illumination.

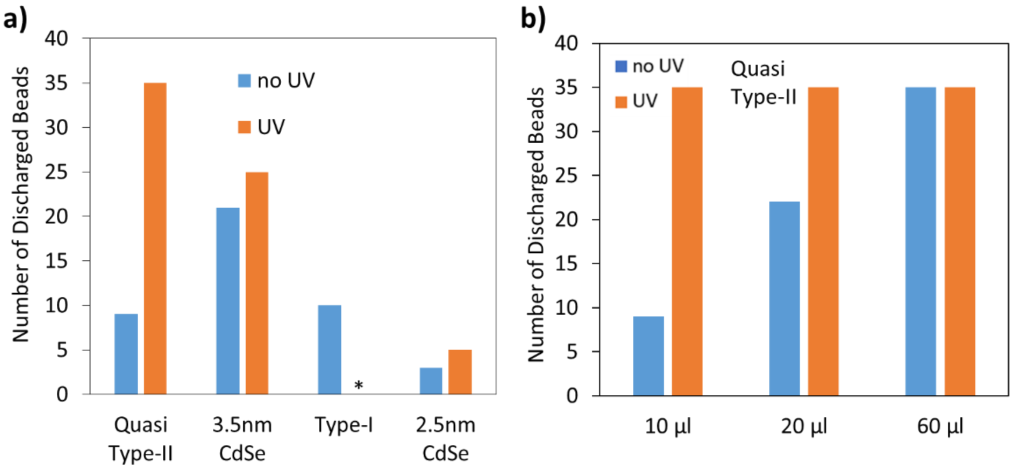

**Figure 6.9.** a) The number of discharged beads (N=35) in the first 5 minutes after the QD solution was added into the hexane in the glass vial with 35 contact-charged PTFE beads. * indicates the Type-I QDs did not discharged beads in 5 minutes under UV illumination. b) The number of discharged beads in 5 minutes vs added microliters of quasi-type-II QDs in the vials. All of beads discharged in 5 minutes in UV illumination.

The case with the type-I QD solutions in the dark was similar to those with quasi-type-II: the beads started to discharge immediately after the solution addition to the vial. A quantitative comparison showing slight differences in the number of beads discharging in the first five minutes after the solution injection is given in **Figure 6.9**. Again, an interesting result popped out when the type-I QD solution was injected into the vial under illumination – *no beads discharged* in this case, similar to the control sample, where only the same amount of hexane was added.

## 6.3 Discussion

### 6.3.1 The Effect of The Core QDs on the Dissipation of Contact Charges

As shown in **Figure 6.7**, the core CdSe nanocrystals are ineffective in dissipation of charged PDMS's contact charges when doped in PDMS. The reason for this ineffectiveness could be the ease of oxidation of CdSe nanocrystals which may have taken place during sample preparation and doping into the polymers. The third component ($\tau_3$) indicates the presence of deep trap states in CdSe QDs (2.5 nm and 3.5 nm), which was shown in **Figure 6.2a** [117] (During the PL measurements, the contact of the QD solutions with air was inevitable; therefore, core QD surface may get oxidized). The presence of these charge trap states on the QD surface and other crystal defects may lead to Auger recombination and oxidation on the nanocrystal surface [113], [114], [115], [116]. Another indication that the oxidation might be the reason for nondischarging QDs comes from the increased discharging efficiencies of the QDs in solution experiments. In these experiments, anhydrous hexane provided a suitable nonpolar medium, and prior degassing helped to remove the oxygen. Therefore, oxidation is prevented, and the QDs show some discharging behavior.

*The effect of illumination.* As shown in the introduction, the electron and hole pairs are generated when QDs are exposed to light. Our hypothesis was; that the $e^-/h^+$ pair generated should interact with the mechanospecies (charge bearing mechanoanions and mechanocations) developed on the polymer surface to provide pathways to the charge dissipation. However, this was not the case for the core QDs doped into the PDMS, presumably because of the surface oxidation discussed above.

In the solvent, however, where oxidation is prevented, these charge carriers ($e^-$ and $h^+$) interact with the mechanospecies after their formation to mediate the dissipation of charges on them. The $e^-/h^+$ pair generation takes place to some extent; even no additional UV illumination is provided (under ambient light) due to the broad absorption characteristics of QDs. Therefore, the fast dissipation mediated by the $e^-/h^+$ pair may occur even under ambient light conditions. When the vials of charged polymer beads in hexane, injected with 2.5 nm and 3.5 nm CdSe solutions, were exposed to UV light, the excited state population of the charge carriers takes place, and an enhanced discharging effect is observed because of the increased number of electron-hole pairs in the excited state.

### 6.3.2 The Core/Shell Effect on the Dissipation of Contact Charges

Shell growth is known to reduce the number of trap states such as dangling bonds on the surface of QDs and Auger recombination, causing an increase in the fluorescence quantum yield (QY), and the electron/hole transfer rates in the system [113], [114], [115], [116]. With our QDs, when the cores are passivated, the third component of the lifetime has not been observed in the PL of the core/shell nanocrystals. Therefore, the surfaces can be said to be passivated by the inorganic ZnSe shell. Also, QY of core/shell increases dramatically compared to only core QDs. Compared to the case where we used the core CdSe nanocrystals for doping, the discharging effect boosts when surface-passivated core/shell QDs are dispersed in the polymer matrix. Here, as expected, the formed $e^-/h^+$ pair can take place in the charge dissipation, interacting with mechanospecies.

*The effect of illumination.* After we determined the QY values for the core/shell QDs, we hypothesized that the QDs with higher QY should yield a better dissipation of contact charges. We suspected this behavior since QY measures how well an $e^-/h^+$ pair is sustained in a QD. So Type-I (QY=58.49%) should dominate the quasi-type-II (QY=27.43%). We observed that when the quasi-type-II QD doped polymer sample was illuminated by UV light, the decay rate increased compared to the no UV condition. However, surprisingly, Type-1 showed a decrease in the decay rate with UV illumination. This led to us thinking about a 'charge carrier localization effect', as described below.

### 6.3.3 The Charge Carrier Localization Effect on the Dissipation of Contact Charges

Directed by the results of the discharging experiments, the dissipation of contact charges on polymers mediated by core/shell nanocrystals in solid and solvent systems can be surmised with a mechanism shown in **Figure 6.10**.

First, when a QD-doped PDMS polymer is contact-charged with Aluminum, nonequilibrium electron-hole pairs are created because of friction energy on the surface of QDs [118], [119], [120], [121] **(1)**. We propose that the nonequilibrium carriers are created on the ZnSe surface, and they interact with the mechanospecies **(2)**. Mechanoanions donate their electrons to the holes on the ZnSe surface. After that, they become mechanoradicals, and further electron transfer from mechanoanions generates mechanocations. Therefore, the overall effect is the decrease in the magnitude of negative triboelectric charges. On the other hand, there is a possibility of electron transfer from the ZnSe shell to the mechanocations, which converts them to mechanoradicals, and mechanoanions are formed by further electron transfer. Type-I and quasi-type-II core/shell QDs having the same shell materials (ZnSe) and the same thickness (3 ML) showed a similar decay rate in dark conditions (**Figure 6.7**). Therefore, these results indicate that the electron and hole transfer mechanism controls overall charge dissipation.

When a type-I doped PDMS sample is exposed to light after tribocharging **(1)**, an initial electron-hole pair is created on CdSe **(3)** and ZnSe shells. Electrons and holes generated on the ZnSe shell transfer to the core **(4)**. The electron-hole pair caused by light might recombine in the CdSe core **(5)** and possibly with the electron/hole on the ZnSe shell. These recombination processes decrease the population of electrons and holes on the ZnSe shell and crystal surface. Therefore, positive charge carriers on the crystal surface disappear quickly. Hence, the decay rate slows for type-I doped polymer samples under UV illumination due to the more prolonged survival of negative triboelectric charges on the PDMS surface. For quasi-type-II, the holes delocalize on the core or the shell. When exposed to UV, the holes transferred to the nanocrystal surface **(4)** interact with mechanoanions causing fast charge dissipation. The discharging effect depends on the population of holes on the surface. PDMS has overall negative charges, and its dissipation depends on the interaction between mechanoanions and positive charge carriers ($h^+$).

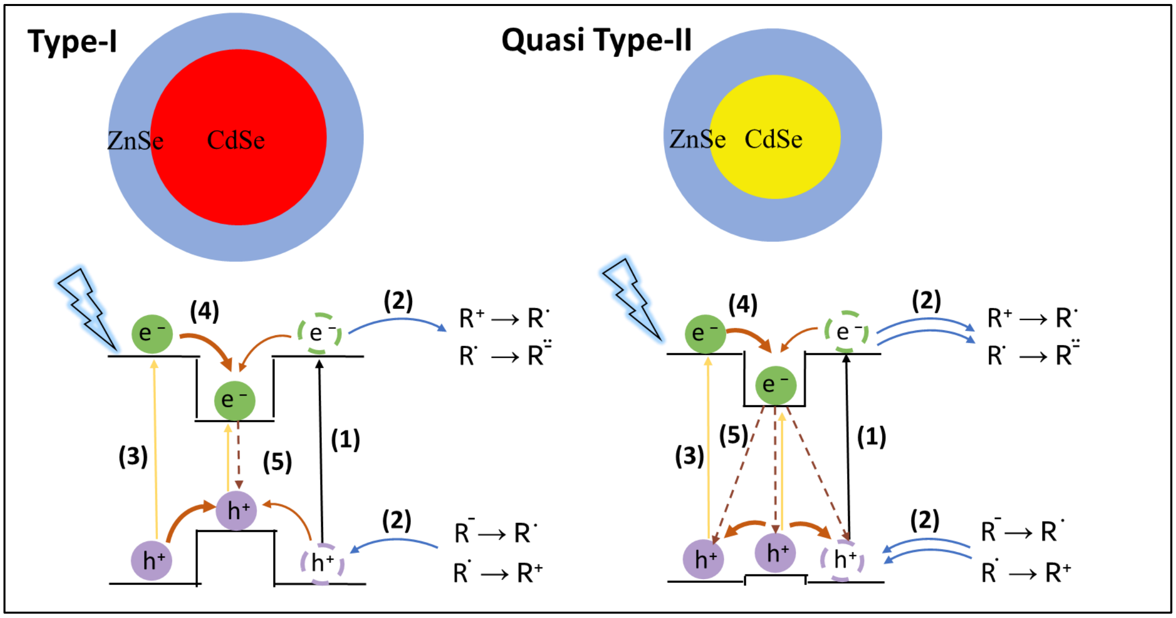

**Figure 6.10**. The proposed mechanism of the interaction of the different heterostructures of core/shell QD effect with the mechanospecies.

Unlike in the polymer system, the QDs were added into the hexane where PTFE beads were already tribocharged, and there are only mechanoanions/mechanoradicals on the PTFE surface. Therefore, there are no 'nonequilibrium carriers' generated on the QD surface due to friction energy. Static charge is dissipated by the interaction with PTFE$^-$ and the electron-hole pair with QDs. Type-I has localized electrons and holes in the core. The shell blocks the interaction of the pair with the species in the environment (mechanoanions) in Type-I [122], [123]. Thus, the interaction of positive charge carriers on the surface with mechanoanions is reduced in ambient conditions compared to its bare core. When the solution with charged beads is exposed to UV light, recombination processes are active, and discharging effect is dramatically reduced. On the other hand, quasi-type-II having delocalized holes on the crystal surface enables discharging of the beads rapidly. This effect is enhanced under the illumination of UV light because the population of electron and hole pair is increased.

## 6.4. Conclusion (Part B)

We report;

1) The dissipation of contact charges on a polymer (PDMS) doped with QDs is dependent on the type of QD (core or core/shell).

2) The dissipation observed in the presence of QDs can further be facilitated or decreased by photoexcitation of the samples; the result depends on the QD type.

3) The type and **illumination-dependent** QDs suggest that the **electron-hole** pair is interacting with the mechanospecies on the polymers.

With all these findings, we propose a novel charge control method using QDs in common polymers as additives. The method uses minute amounts of QDs that can be doped into the polymers, mixing the polymers in the QD solutions. The results promise that the new method can be tuned with all attributes of QD chemistry (chemistry, type, size, shape, etc. of QDs), and can be remotely controlled by light.

# Chapter 7

## References

1. Zhang, R., Hummelgård, M., Örtegren, J., Olsen, M., Andersson, H., Yang, Y., Zheng H., & Olin, H. (2021). The triboelectricity of the human body. Nano Energy, 86, 106041.
2. Loeb, L. B. (1945). The basic mechanisms of static electrification. Science, 102(2658), 573-576
3. Chen, L., Shi, Q., Sun, Y., Nguyen, T., Lee, C., & Soh, S. (2018). Controlling surface charge generated by contact electrification: strategies and applications. Advanced Materials, 30(47), 1802405.
4. Fan, F. R., Tian, Z. Q., & Wang, Z. L. (2012). Flexible triboelectric generator. Nano energy, 1(2), 328-334.
5. Schein, L. B. (2013). Electrophotography and development physics (Vol. 14). Springer Science & Business Media.
6. Bailey, A. G. (1998). The science and technology of electrostatic powder spraying, transport and coating. Journal of electrostatics, 45(2), 85-120.
7. Cruz, C. F., Costa, C., Gomes, A. C., Matamá, T., & Cavaco-Paulo, A. (2016). Human hair and the impact of cosmetic procedures: a review on cleansing and shape-modulating cosmetics. Cosmetics, 3(3), 26.
8. J. C. Wilcke, Disputatio Physica Experimentalis, De Electricitatibus Contrariis, Rostochii: Typis Ioannis Iacobi Adleri, 1757.
9. Shaw, P. E. (1917). Experiments on tribo-electricity. I.—The tribo-electric series. Proceedings of the Royal Society of London. Series A, Containing Papers of a Mathematical and Physical Character, 94(656), 16-33.
10. Galembeck, F., Burgo, T. A., Balestrin, L. B., Gouveia, R. F., Silva, C. A., & Galembeck, A. (2014). Friction, tribochemistry and triboelectricity: recent progress and perspectives. Rsc Advances, 4(109), 64280-64298.
11. Ko, H., Lim, Y. W., Han, S., Jeong, C. K., & Cho, S. B. (2021). Triboelectrification: Backflow and Stuck Charges Are Key. ACS Energy Letters, 6(8), 2792-2799.

12. Gupta, R., Gidaspow, D., & Wasan, D. T. (1993). Electrostatic separation of powder mixtures based on the work functions of its constituents. Powder Technology, 75(1), 79-87.
13. Lowell, J., & Rose-Innes, A. C. (1980). Contact electrification. Advances in Physics, 29(6), 947-1023.
14. Lowell, J., & Truscott, W. S. (1986). Triboelectrification of identical insulators. II. Theory and further experiments. Journal of Physics D: Applied Physics, 19(7), 1281.
15. Waitukaitis, S. R., Lee, V., Pierson, J. M., Forman, S. L., & Jaeger, H. M. (2014). Size-dependent same-material tribocharging in insulating grains. Physical Review Letters, 112(21), 218001.
16. Abdelaziz, K. M., Chen, J., Hieber, T. J., & Leseman, Z. C. (2018). Atomistic Field Theory for contact electrification of dielectrics. Journal of Electrostatics, 96, 10-15.
17. Liu, J., Goswami, A., Jiang, K., Khan, F., Kim, S., McGee, R., ... & Thundat, T. (2018). Direct-current triboelectricity generation by a sliding Schottky nanocontact on MoS2 multilayers. Nature nanotechnology, 13(2), 112-116.
18. Liu, J., Jiang, K., Nguyen, L., Li, Z., & Thundat, T. (2019). Interfacial friction-induced electronic excitation mechanism for tribo-tunneling current generation. Materials Horizons, 6(5), 1020-1026.
19. Lacks, D. J., & Shinbrot, T. (2019). Long-standing and unresolved issues in triboelectric charging. Nature Reviews Chemistry, 3(8), 465-476.
20. Knoblauch, O. (1902). Versuche über die Berührungselektrizität. Zeitschrift für Physikalische Chemie, 39(1), 225-244.
21. Medley, J. A. (1953). Fractional electrification of polar polymers. Nature, 171(4363), 1077-1077.
22. Diaz, A. F., & Felix-Navarro, R. M. (2004). A semi-quantitative tribo-electric series for polymeric materials: the influence of chemical structure and properties. Journal of Electrostatics, 62(4), 277-290.
23. Harper, W. R. (1998). Contact and frictional electrification. Morgan Hill.
24. Medley, J. A. (1953). Fractional electrification of polar polymers. Nature, 171(4363), 1077-1077.

25. Diaz, A. F. (1998). Contact electrification of materials: the chemistry of ions on polymer surfaces. The Journal of Adhesion, 67(1-4), 111-122.
26. Gouveia, R. F., & Galembeck, F. (2009). Electrostatic charging of hydrophilic particles due to water adsorption. Journal of the American chemical society, 131(32), 11381-11386.
27. Ducati, T. R., Simoes, L. H., & Galembeck, F. (2010). Charge partitioning at gas− solid interfaces: Humidity causes electricity buildup on metals. Langmuir, 26(17), 13763-13766.
28. Gouveia, R. F., & Galembeck, F. (2009). Electrostatic charging of hydrophilic particles due to water adsorption. Journal of the American chemical society, 131(32), 11381-11386.
29. McCarty, L. S., & Whitesides, G. M. (2008). Electrostatic charging due to separation of ions at interfaces: contact electrification of ionic electrets. Angewandte Chemie International Edition, 47(12), 2188-2207.
30. Homewood, K. P. (1981). Do 'dirty'surfaces matter in coBaytekin, H. T., Baytekin, B., Soh, S., & Grzybowski, B. A. (2011).
31. Is water necessary for contact electrification?. Angewandte Chemie, 123(30), 6898-6902.ntact electrification experiments?. Journal of Electrostatics, 10, 299-304.
32. Harper, W. R. (1967). Contact and frictional electrification. Clarendon P..
33. Salaneck, W. R., Paton, A., & Clark, D. T. (1976). Double mass transfer during polymer-polymer contacts. Journal of Applied Physics, 47(1), 144-147.
34. Lowell, J. (1977). The role of material transfer in contact electrification. Journal of Physics D: Applied Physics, 10(17), L233.
35. Baytekin, H. T., Baytekin, B., Incorvati, J. T., & Grzybowski, B. A. (2012). Material transfer and polarity reversal in contact charging. Angewandte Chemie International Edition, 51(20), 4843-4847.
36. Henniker, J. (1962). Triboelectricity in polymers. Nature, 196(4853), 474-474.
37. Sakaguchi, M., & Sohma, J. (1975). Anomalous Decay Behavior of the Polypropylene Radicals Produced by Mechanical Fracture: Effect of the Excess Charges Due to Triboelectricity. Polymer Journal, 7(4), 490-497.

38. Baytekin, H. T., Baytekin, B., Hermans, T. M., Kowalczyk, B., & Grzybowski, B. A. (2013). Control of surface charges by radicals as a principle of antistatic polymers protecting electronic circuitry. Science, 341(6152), 1368-1371.
39. Sakaguchi, M., Makino, M., Ohura, T., & Iwata, T. (2014). Contact electrification of polymers due to electron transfer among mechano anions, mechano cations and mechano radicals. Journal of Electrostatics, 72(5), 412-416.
40. Baytekin, H. T., Patashinski, A. Z., Branicki, M., Baytekin, B., Soh, S., & Grzybowski, B. A. (2011). The mosaic of surface charge in contact electrification. Science, 333(6040), 308-312.
41. Burgo, T. A., Ducati, T. R., Francisco, K. R., Clinckspoor, K. J., Galembeck, F., & Galembeck, S. E. (2012). Triboelectricity: macroscopic charge patterns formed by self-arraying ions on polymer surfaces. Langmuir, 28(19), 7407-7416.
42. Sherrell, P. C., Sutka, A., Shepelin, N. A., Lapcinskis, L., Verners, O., Germane, L., ... & Ellis, A. V. (2021). Probing contact electrification: a cohesively sticky problem. ACS Applied Materials & Interfaces, 13(37), 44935-44947.
43. Tolinski, M. (2015). Additives for polyolefins: getting the most out of polypropylene, polyethylene and TPO. William Andrew.
44. Rosner, R. B. (2001). Conductive materials for ESD applications: an overview. IEEE transactions on device and materials reliability, 1(1), 9-16.
45. Fenzel-Alexander, D., Brock, P., & Diaz, A. (1994). Control of contact charge in polymers with ionomers. Langmuir, 10(9), 3323-3327.
46. Burgo, T. A. L., Balestrin, L. B. S., & Galembeck, F. (2014). Corona charging and potential decay on oxidized polyethylene surfaces. Polymer degradation and stability, 104, 11-17.
47. Baytekin, H. T., Baytekin, B., Hermans, T. M., Kowalczyk, B., & Grzybowski, B. A. (2013). Control of surface charges by radicals as a principle of antistatic polymers protecting electronic circuitry. Science, 341(6152), 1368-1371.
48. Fang, Y., Gonuguntla, S., & Soh, S. (2017). Universal nature-inspired coatings for preparing noncharging surfaces. ACS applied materials & interfaces, 9(37), 32220-32226.

49. Zhang, X., Huang, X., Kwok, S. W., & Soh, S. (2016). Designing non-charging surfaces from non-conductive polymers. Advanced materials, 28(15), 3024-3029.
50. Özel, M., Demir, F., Aikebaier, A., Kwiczak-Yiğitbaşı, J., Baytekin, H. T., & Baytekin, B. (2020). Why does wood not get contact charged? lignin as an antistatic additive for common polymers. Chemistry of Materials, 32(17), 7438-7444.
51. Cezan, S. D., Nalbant, A. A., Buyuktemiz, M., Dede, Y., Baytekin, H. T., & Baytekin, B. (2019). Control of triboelectric charges on common polymers by photoexcitation of organic dyes. Nature communications, 10(1), 1-8.
52. Balpande, S., & Pande, S. (2022). Comparative Evaluation of Fabric Yarn, Polymers, and Seed Crust Dielectrics for Triboelectric Energy Harvesters. Journal of Electronic Materials, 1-11.
53. Occupational Safety and Health Administration (OSHA), https://www.osha.gov/dsg/combustibledust/index.html.
54. Mehrotra, A., Muzzio, F. J., & Shinbrot, T. (2007). Spontaneous separation of charged grains. Physical review letters, 99(5), 058001.
55. Sayyah, A., Horenstein, M. N., & Mazumder, M. K. (2014). Energy yield loss caused by dust deposition on photovoltaic panels. Solar Energy, 107, 576-604.
56. Vinson, J. E., & Liou, J. J. (1998). Electrostatic discharge in semiconductor devices: an overview. Proceedings of the IEEE, 86(2), 399-420.
57. Walmsley, H. L. (1982). The generation of electric currents by the turbulent flow of dielectric liquids. I. Long pipes. Journal of Physics D: Applied Physics, 15(10), 1907.
58. Musa, U. G., Cezan, S. D., Baytekin, B., & Baytekin, H. T. (2018). The charging events in contact-separation electrification. Scientific reports, 8(1), 1-8.
59. Zhao, Y., & Truhlar, D. G. (2008). The M06 suite of density functionals for main group thermochemistry, thermochemical kinetics, noncovalent interactions, excited states, and transition elements: two new functionals and systematic testing of four M06-class functionals and 12 other functionals. Theoretical chemistry accounts, 120(1), 215-241.
60. Frisch, M. J.; Trucks, G. W.; Schlegel, H. B.; Scuseria, G. E.; Robb, M. A.; Cheeseman, J. R.; Scalmani, G.; Barone, V.; Mennucci, B.; Petersson, G. A.; Nakatsuji, H.; Caricato, M.; Li, X.; Hratchian, H. P.; Izmaylov, A. F.; Bloino, J.; Zheng, G.; Sonnenberg, J. L.; Hada, M.; Ehara, M.; Toyota, K.; Fukuda, R.; Hasegawa, J.; Ishida, M.; Nakajima, T.;

Honda, Y.; Kitao, O.; Nakai, H.; Vreven, T.; Montgomery, J. A., Jr.; Peralta, J. E.; Ogliaro, F.; Bearpark, M.; Heyd, J. J.; Brothers, E.; Kudin, K. N.; Staroverov, V. N.; Kobayashi, R.; Normand, J.; Raghavachari, K.; Rendell, A.; Burant, J. C.; Iyengar, S. S.; Tomasi, J.; Cossi, M.; Rega, N.; Millam, J. M.; Klene, M.; Knox, J. E.; Cross, J. B.; Bakken, V.; Adamo, C.; Jaramillo, J.; Gomperts, R.; Stratmann, R. E.; Yazyev, O.; Austin, A. J.; Cammi, R.; Pomelli, C.; Ochterski, J. W.; Martin, R. L.; Morokuma, K.; Zakrzewski, V. G.; Voth, G. A.; Salvador, P.; Dannenberg, J. J.; Dapprich, S.; Daniels, A. D.; Farkas, Ö.; Foresman, J. B.; Ortiz, J. V.; Cioslowski, J.; Fox, D. J. Gaussian, Inc., Wallingford CT, 2009.

61. Singh, U.C.; Kollman, P.A. An approach to computing electrostatic charges for molecules. J. Comput. Chem. 1984, 5, 129–145.
62. Reed, A. E., Weinstock, R. B., & Weinhold, F. (1985). Natural population analysis. The Journal of chemical physics, 83(2), 735-746.
63. Kistenmacher, T. J., Emge, T. J., Bloch, A. N., & Cowan, D. O. (1982). Structure of the red, semiconducting form of 4, 4', 5, 5'-tetramethyl-Δ2, 2'-bi-1, 3-diselenole-7, 7, 8, 8-tetracyano-p-quinodimethane, TMTSF–TCNQ. Acta Crystallographica Section B: Structural Crystallography and Crystal Chemistry, 38(4), 1193-1199.
64. R. L. Martin, “Natural transition orbitals,” J. Chem. Phys., 118 (2003) 4775-77. DOI: 10.1063/1.1558471.
65. Wöhler, F. (1844). Untersuchungen über das Chinon (Vol. 2).
66. FERRARIS J.P., COWAN DO., WALATKA V. and PERLSTEIN J.H. (1973). J. Am. Chem. Soc. 95, 948 (1973).
67. Odom, S. A., Caruso, M. M., Finke, A. D., Prokup, A. M., Ritchey, J. A., Leonard, J. H., ... & Moore, J. S. (2010). Restoration of conductivity with TTF-TCNQ charge-transfer salts. Advanced Functional Materials, 20(11), 1721-1727.
68. Hu, P., Ye, J., He, X., Du, K., Zhang, K. K., Wang, X., ... & Kloc, C. (2016). Control of radiative exciton recombination by charge transfer induced surface dipoles in MoS2 and WS2 monolayers. Scientific reports, 6(1), 1-8.
69. Eldaroti, H. H., Gadir, S. A., Refat, M. S., & Adam, A. M. A. (2014). Charge-transfer interaction of drug quinidine with quinol, picric acid and DDQ: Spectroscopic

characterization and biological activity studies towards understanding the drug–receptor mechanism. Journal of Pharmaceutical Analysis, 4(2), 81-95.

70. Schein, L.B., & Czanderna, K.K. (1988). Electrophotography and Development Physics.
71. Shen, D., Chen, W. C., Lo, M. F., & Lee, C. S. (2021). Charge-transfer complexes and their applications in optoelectronic devices. Materials Today Energy, 20, 100644.
72. Acker, D. S., & Hertler, W. R. (1962). Substituted quinodimethans. I. Preparation and chemistry of 7, 7, 8, 8-tetracyanoquinodimethan. Journal of the American Chemical Society, 84(17), 3370-3374.
73. Tseng, T. C., Urban, C., Wang, Y., Otero, R., Tait, S. L., Alcamí, M., ... & Miranda, R. (2010). Charge-transfer-induced structural rearrangements at both sides of organic/metal interfaces. Nature Chemistry, 2(5), 374-379.
74. Zhang, J., Tan, J., Ma, Z., Xu, W., Zhao, G., Geng, H., ... & Zhu, D. (2013). Fullerene/sulfur-bridged annulene cocrystals: two-dimensional segregated heterojunctions with ambipolar transport properties and photoresponsivity. Journal of the American Chemical Society, 135(2), 558-561.
75. Jiang, H., Hu, P., Ye, J., Zhang, K. K., Long, Y., Hu, W., & Kloc, C. (2018). Tuning of the degree of charge transfer and the electronic properties in organic binary compounds by crystal engineering: a perspective. Journal of Materials Chemistry C, 6(8), 1884-1902.
76. Herbstein, F. H. (2005). Crystalline molecular complexes and compounds: structures and principles (Vol. 18). OUP Oxford.
77. Goetz, K. P., Vermeulen, D., Payne, M. E., Kloc, C., McNeil, L. E., & Jurchescu, O. D. (2014). Charge-transfer complexes: new perspectives on an old class of compounds. Journal of Materials Chemistry C, 2(17), 3065-3076.
78. Yu, W., Wang, X. Y., Li, J., Li, Z. T., Yan, Y. K., Wang, W., & Pei, J. (2013). A photoconductive charge-transfer crystal with mixed-stacking donor–acceptor heterojunctions within the lattice. Chemical Communications, 49(1), 54-56.
79. Gao, J., Zhai, H., Hu, P., & Jiang, H. (2020). The stoichiometry of TCNQ-based organic charge-transfer cocrystals. Crystals, 10(11), 993.

80. Park, S. K., Kim, J. H., & Park, S. Y. (2018). Organic 2D optoelectronic crystals: charge transport, emerging functions, and their design perspective. Advanced Materials, 30(42), 1704759.
81. Li, J., Shepelin, N. A., Sherrell, P. C., & Ellis, A. V. (2021). Poly (dimethylsiloxane) for triboelectricity: From mechanisms to practical strategies. Chemistry of Materials, 33(12), 4304-4327.
82. Bender, C. J. (1986). Theoretical models of charge-transfer complexes. Chemical Society Reviews, 15(4), 475-502.
83. Krawczyk, S., Nawrocka, A., & Zdyb, A. (2018). Charge-transfer excited state in pyrene-1-carboxylic acids adsorbed on titanium dioxide nanoparticles. Spectrochimica Acta Part A: Molecular and Biomolecular Spectroscopy, 198, 19-26.
84. Zhu, L., Kim, E. G., Yi, Y., & Brédas, J. L. (2011). Charge transfer in molecular complexes with 2, 3, 5, 6-tetrafluoro-7, 7, 8, 8-tetracyanoquinodimethane (F4-TCNQ): A density functional theory study. Chemistry of Materials, 23(23), 5149-5159.
85. Mahato, S., Puigdollers, J., Voz, C., Mukhopadhyay, M., Mukherjee, M., & Hazra, S. (2020). Near 5% DMSO is the best: A structural investigation of PEDOT: PSS thin films with strong emphasis on surface and interface for hybrid solar cell. Applied Surface Science, 499, 143967.
86. Wei, Q., Mukaida, M., Naitoh, Y., & Ishida, T. (2013). Morphological change and mobility enhancement in PEDOT: PSS by adding co - solvents. Advanced materials, 25(20), 2831-2836.
87. Talapin, D. V., Lee, J. S., Kovalenko, M. V., & Shevchenko, E. V. (2010). Prospects of colloidal nanocrystals for electronic and optoelectronic applications. Chemical reviews, 110(1), 389-458.
88. Ko, J., Jeong, B. G., Chang, J. H., Joung, J. F., Yoon, S. Y., Lee, D. C., ... & Bang, J. (2020). Chemically resistant and thermally stable quantum dots prepared by shell encapsulation with cross-linkable block copolymer ligands. NPG Asia Materials, 12(1), 1-11.
89. Zhang, Y., Wu, G., Liu, F., Ding, C., Zou, Z., & Shen, Q. (2020). Photoexcited carrier dynamics in colloidal quantum dot solar cells: insights into individual quantum dots, quantum dot solid films and devices. Chemical Society Reviews, 49(1), 49-84.

90. Cotta, M. A. (2020). Quantum dots and their applications: what lies ahead? ACS applied nano materials, 3(6), 4920-4924.
91. Chen, G., Seo, J., Yang, C., & Prasad, P. N. (2013). Nanochemistry and nanomaterials for photovoltaics. Chemical Society Reviews, 42(21), 8304-8338.
92. Park, Y., Jeong, S., & Kim, S. (2017). Medically translatable quantum dots for biosensing and imaging. Journal of Photochemistry and Photobiology C: Photochemistry Reviews, 30, 51-70.
93. Devi, S., & Tharmaraj, V. (2020). Quantum Dots in Green Photocatalytic Applications for Degradation of Environmental Pollutants and Hydrogen Evolution. In Green Photocatalysts for Energy and Environmental Process (pp. 87-108). Springer, Cham.
94. Liu, L., Cheng, Y., Zhu, L., Lee, S. T., Liao, F., & Shao, M. (2016). The surface polarized graphene oxide quantum dot films for flexible nanogenerators. Scientific reports, 6(1), 1-7.
95. Choi, G. J., Baek, S. H., Lee, S. S., Khan, F., Kim, J. H., & Park, I. K. (2019). Performance enhancement of triboelectric nanogenerators based on polyvinylidene fluoride/graphene quantum dot composite nanofibers. Journal of Alloys and Compounds, 797, 945-951.
96. Alivisatos, A. P. (1996). Semiconductor clusters, nanocrystals, and quantum dots. science, 271(5251), 933-937.
97. Vokhmintcev, K. V., Samokhvalov, P. S., & Nabiev, I. (2016). Charge transfer and separation in photoexcited quantum dot-based systems. Nano Today, 11(2), 189-211
98. Zhao, K., Pan, Z., Mora-Seró, I., Cánovas, E., Wang, H., Song, Y., ... & Zhong, X. (2015). Boosting power conversion efficiencies of quantum-dot-sensitized solar cells beyond 8% by recombination control. Journal of the American Chemical Society, 137(16), 5602-5609.
99. Jiang, Z. J., & Kelley, D. F. (2011). Hot and relaxed electron transfer from the CdSe core and core/shell nanorods. The Journal of Physical Chemistry C, 115(11), 4594-4602.
100. Murray, C., Norris, D. J., & Bawendi, M. G. (1993). Synthesis and characterization of nearly monodisperse CdE (E= sulfur, selenium, tellurium) semiconductor nanocrystallites. Journal of the American Chemical Society, 115(19), 8706-8715.

101. LaMer, V. K., & Dinegar, R. H. (1950). Theory, production and mechanism of formation of monodispersed hydrosols. Journal of the american chemical society, 72(11), 4847-4854.

102. Pradhan, N., & Efrima, S. (2003). Single-precursor, one-pot versatile synthesis under near ambient conditions of tunable, single and dual band fluorescing metal sulfide nanoparticles. Journal of the American Chemical Society, 125(8), 2050-2051.

103. Cumberland, S. L., Hanif, K. M., Javier, A., Khitrov, G. A., Strouse, G. F., Woessner, S. M., & Yun, C. S. (2002). Inorganic clusters as single-source precursors for preparation of CdSe, ZnSe, and CdSe/ZnS nanomaterials. Chemistry of Materials, 14(4), 1576-1584.

104. Li, J. J., Wang, Y. A., Guo, W., Keay, J. C., Mishima, T. D., Johnson, M. B., & Peng, X. (2003). Large-scale synthesis of nearly monodisperse CdSe/CdS core/shell nanocrystals using air-stable reagents via successive ion layer adsorption and reaction. Journal of the American Chemical Society, 125(41), 12567-12575.

105. Tong, X., & Wang, Z. M. (2020). Core/Shell Quantum Dots. Springer International Publishing.

106. Pietryga, J. M., Park, Y. S., Lim, J., Fidler, A. F., Bae, W. K., Brovelli, S., & Klimov, V. I. (2016). Spectroscopic and device aspects of nanocrystal quantum dots. Chemical reviews, 116(18), 10513-10622.

107. Singh, S., Garg, S., & Saran, A. D. (2021). Photocatalytic activity of CdS and CdSe quantum dots for degradation of 3-aminopyridine. Nanotechnology for Environmental Engineering, 6(3), 1-8.

108. Huang, F., Zhang, Q., Xu, B., Hou, J., Wang, Y., Massé, R. C., ... & Cao, G. (2016). A comparison of ZnS and ZnSe passivation layers on CdS/CdSe co-sensitized quantum dot solar cells. Journal of Materials Chemistry A, 4(38), 14773-14780.

109. Acharya, K. P., Nguyen, H. M., Paulite, M., Piryatinski, A., Zhang, J., Casson, J. L., ..& Hollingsworth, J. A. (2015). Elucidation of two giants: challenges to thick-shell synthesis in CdSe/ZnSe and ZnSe/CdS core/shell quantum dots. Journal of the American Chemical Society, 137(11), 3755-3758.

110. Kudilatt, H., Hou, B., & Welland, M. E. (2020). Quantum Dots Microstructural Metrology: From Time-Resolved Spectroscopy to Spatially Resolved Electron Microscopy. Particle & Particle Systems Characterization, 37(12), 2000192

111. Dargahzadeh, M., Molaei, M., & Karimipour, M. (2018). Completely quenching of the trap states emission of CdSe QDs by CdS/ZnS shell growth using a one pot photochemical approach and application for dye photo-degradation. Journal of Luminescence, 203, 723-729.

112. Heydaripour, F., Molaei, M., Karimipour, M., Dehghan, F., & Mollahosseini, E. (2019). Conversion of the yellow to blue emission of CdSe quantum dots (QDs) via ZnSe shell growth. Journal of Materials Science: Materials in Electronics, 30(12), 11378-11382.

113. Vokhmintcev, K. V., Samokhvalov, P. S., & Nabiev, I. (2016). Charge transfer and separation in photoexcited quantum dot-based systems. Nano Today, 11(2), 189-211.

114. Zhao, K., Pan, Z., Mora-Seró, I., Cánovas, E., Wang, H., Song, Y., ... & Zhong, X. (2015). Boosting power conversion efficiencies of quantum-dot-sensitized solar cells beyond 8% by recombination control. Journal of the American Chemical Society, 137(16), 5602-5609.

115. Jiang, Z. J., & Kelley, D. F. (2011). Hot and relaxed electron transfer from the CdSe core and core/shell nanorods. The Journal of Physical Chemistry C, 115(11), 4594-4602.

116. Reiss, P., Protiere, M., & Li, L. (2009). Core/shell semiconductor nanocrystals. small, 5(2), 154-168.

117. Kudilatt, H., Hou, B., & Welland, M. E. (2020). Quantum Dots Microstructural Metrology: From Time-Resolved Spectroscopy to Spatially Resolved Electron Microscopy. Particle & Particle Systems Characterization, 37(12), 2000192.

118. Liu, J., Goswami, A., Jiang, K., Khan, F., Kim, S., McGee, R., ... & Thundat, T. (2018). Direct-current triboelectricity generation by a sliding Schottky nanocontact on MoS2 multilayers. Nature nanotechnology, 13(2), 112-116.

119. Liu, J., Jiang, K., Nguyen, L., Li, Z., & Thundat, T. (2019). Interfacial friction-induced electronic excitation mechanism for tribo-tunneling current generation. Materials Horizons, 6(5), 1020-1026.

120. Zhang, Z., Jiang, D., Zhao, J., Liu, G., Bu, T., Zhang, C., & Wang, Z. L. (2020). Tribovoltaic effect on metal–semiconductor interface for direct-current low-impedance triboelectric nanogenerators. Advanced Energy Materials, 10(9), 1903713.

121. Yang, B., Chen, H., Guo, X., Wang, L., Xu, T., Bian, J., ... & Lou, X. (2020). Enhanced tribocatalytic degradation using piezoelectric CdS nanowires for efficient water remediation. Journal of Materials Chemistry C, 8(42), 14845-14854.

122. Mélinon, P., Begin-Colin, S., Duvail, J. L., Gauffre, F., Boime, N. H., Ledoux, G., ... & Warot-Fonrose, B. (2014). Engineered inorganic core/shell nanoparticles. Physics Reports, 543(3), 163-197.

123. Yadav, S., Chowdhury, A., & Sapra, S. (2016). Thickness-Dependent Charge Carrier Dynamics in CdSe/ZnSe/CdS Core/Barrier/Shell Nanoheterostructures. ChemPhysChem, 17(5), 692-698.